Physics – Uspekhi **66** (10) 967 – 986 (2023)

REVIEWS OF TOPICAL PROBLEMS PACS numbers: **91.25. – r, 94.30. – d,** 96.12.Hg

Magnetic field in the inner near-Earth space

V V Malakhov, V V Alekseev, V S Golubkov, A G Mayorov, S A Rodenko, R F Yulbarisov

DOI: https://doi.org/10.3367/UFNe.2022.12.039293

Contents

Abstract. We review the development of modern models of the magnetic field of Earth's inner magnetosphere, from the selection of experimental results to the approximation and presentation of the model output data. In particular, we discuss all principal sources of the magnetic field, their description in various models, and approaches to parameterizing the field. We briefly recall the history of the study of Earth's magnetic field and discuss modern-day and earlier experimental data used in model building and the underlying core mathematical tools. The main features of the majority of modern models describing Earth's magnetic field in the inner magnetosphere are discussed.

Keywords: Earth's inner magnetosphere, Earth's magnetic field models, main magnetic field, lithospheric magnetic field, secular variation, cosmic rays, IGRF, CHAOS

1. Introduction

Earth's magnetic field (EMF in what follows), present in Earth's near magnetosphere, plays a significant role in planning, conducting, and analyzing data from space experiments in low-Earth orbits. First of all, this concerns experiments studying cosmic rays, because, being an obstacle on the path of charged particles to a detector on Earth's surface or in low-Earth orbit, it naturally distorts the recorded (spatial and energy) distributions, separates their fluxes into components, and generally complicates their structure in near-Earth space. One way or another, information about the magnetic field is used in problems such as the separation of the primary, albedo, and trapped components of cosmic rays [1–3], calculation of the geomagnetic cutoff [4, 5], tracing of charged particles in near-Earth space [6], and studying solar–terrestrial connections [7], and is also the most important component of models of the radiation environment [8, 9]. In addition, the magnetic field itself can serve as a tool for particle separation [10].

At the same time, research groups involved in cosmic ray studies pay little attention to the analysis of the existing EMF models and their selection. In the vast majority of cases, only two models are used, the International Geomagnetic Reference Field (IGRF) for the inner magnetosphere and the Tsyganenko model for the outer one. However, the range of tools for modeling EMF is currently very wide, and there are many models (see Table) that may be more suitable for certain tasks. For example, the accuracy of reconstructing the direction of particle motion in modern spectrometers is such that, when tracing them in near-Earth space, in addition to the main and external fields, the contributions of other (lithospheric and ionospheric) components become important, which are absent in the IGRF model. In addition, data from cosmic ray experiments could possibly help in further verifications of EMF models.

In research fields where EMF models are used for auxiliary calculations, a general understanding of the particular features of current EMF studies and related problems seems extremely useful. This topic is covered within due scope in [11], where the authors, in particular, discuss the main sources of magnetic fields and the procedures for obtaining and processing experimental data and describe the use of magnetic field models for solving technological problems.

V V Malakhov [(1, a)], **V V Alekseev** [(2)], **V S Golubkov** [(1)], **A G Mayorov** [(1)], **S A Rodenko** [(1)], **R F Yulbarisov** [(1)]
[(1)] National Research Nuclear University MEPhI, Kashirskoe shosse 31, 115409 Moscow, Russian Federation,
[(2)] Demidov Yaroslavl State University, ul. Sovetskaya 14, 150003 Yaroslavl, Russian Federation
E-mail: [(a)] vvmalakhov@mephi.ru

Received 8 September 2022, revised 1 December 2022
Uspekhi Fizicheskikh Nauk **193** (10) 1025 – 1046 (2023)
Translated by S Alekseev

Table. Characteristics of magnetic field models.*

Component, model	IGRF [112]	WMM [110]	CHAOS [27]	CM [111]	Mag.num [113]	BGS [114]	COV-OBS [115]	gUFM [57]	C^{3}FM [33]	Kalmag [116]	POMME [117]	GRIMM [32]
Main field	$\leqslant 13$ ($\leqslant 10$, $\leqslant 8$)[1]	$\leqslant 12$	$\leqslant 20$	$\leqslant 18$	$\leqslant 20$	$\leqslant 15$	$\leqslant 13$	X	$\leqslant 14$	$\leqslant 20$	$\leqslant 15$	$\leqslant 18$
Secular variation in the main field	$\leqslant 8$	$\leqslant 8$	$\leqslant 20$	X	$\leqslant 13$	$\leqslant 13$	$\leqslant 14$	X	$\leqslant 8$	$\leqslant 20$	$\leqslant 16$	$\leqslant 13$
Lithospheric field	X	X	$\leqslant 70$, $\leqslant 185$	$\leqslant 120$	$\leqslant 100$	$\leqslant 55$	X	X	X	$\leqslant 300$	$\leqslant 133$	$\leqslant 30$
External fields	X	X	$\leqslant 2$	$\leqslant 1$	$\leqslant 3$	$\leqslant 1$	$\leqslant 1$	X	X	$\leqslant 15$	$\leqslant 1$	$\leqslant 1$
Ionospheric field	X	X	X	$\leqslant 60/12$	X	X	X	X	X	$\leqslant 50$	X	X
Tidal field	X	X	X	$\leqslant 22$	X	X	X	X	X	X	X	X
Flows on the MCB[2]	X	X	X	X	X	Y[3]	Y	Y	Y	X	X	X
Time interval	1900 – 2025	2019 – 2025	1999 – 2022	1999 – 2020	2013 – 2020	2009 – 2022	1840 – 2020	1600 – 1990	1957 – 2020	1900 – 2026	2000 – 2017	1999 – 2011
Time parameterization	Linear	Linear	B-spline, 6	B-spline, 4	B-spline, 6	B-spline, 6	B-spline, 4	Snapshot	B-spline, 6[4]	Time series	?	B-spline, 6
Distribution form	exe, Fortran, C++, Python, Matlab, online, coeff.	exe, Fortran, C++, Python, Matlab, online, coeff.	Fortran, Matlab, coeff.	Coeff.	Coeff.	exe, Linux	Fortran, coeff.[5]	Fortran	Coeff.	X	C++, coeff.	Coeff.

Note: For magnetic field components, the maximum order of expansion is indicated, or X if the field component is not in the model; Y means that this component is calculated in the model, ?, that information could not be found; in the line *Distribution form*, 'coeff.' means that the model is distributed in the form of expansion coefficients, 'online,' in a web form for interactive calculation.

[1] Maximum degree of decomposition for the respective period before 2000 and before 1965 is indicated in parentheses.

[2] Mantle–core Boundary.

[3] Calculation of fluxes on the MCB is used as an intermediate stage for calculating the secular variation coefficients and, accordingly, predicting the field.

[4] Used in the classical approach (see Section 5.1): C^{3}FM.

[5] In addition to Gauss coefficients, covariance matrices are also given (see Section 5.1): COV-OBS.

Another good example along these lines is review [12], where the authors focus on current challenges in EMF studies.

The subject of this review is the practical aspect of using EMF and, primarily, model building. These ideas are necessary, first and foremost, for understanding the limitations of models and specific features of their practical application, primarily in the field of cosmic rays, but this information is also likely to be useful in other areas related to cosmic measurements.

Our purpose here is to familiarize the reader with the basic principles of building magnetic field models of the inner magnetosphere and with their types. We briefly describe the history of studying EMF and its structure, and then examine modern approaches to its description and modeling in detail. We describe the magnetic field components of Earth's inner magnetosphere such as the main, lithospheric, external, and ionospheric fields, and also discuss their sources and parameterization methods. Most of the modern models are listed and a brief description of their features is given. We note in passing that the problems of generating EMF [13, 14] are not discussed here.

1.1 Brief historical account

The history of the practical use of EMF began with the invention of the compass in ancient China in the period of the second century BCE to the second century CE [15]; the compass, however, was used for a long time for fortune telling and home arrangement in accordance with geomantic principles. Only by the 10th to 11th centuries CE did it find application in maritime navigation, first in China and then in Europe and Arab countries. The first attempts to explain the nature of terrestrial magnetism were made at the end of the 14th century. William Gilbert, experimenting with a Terrella (small Earth) magnetized ball suggested that Earth is a large magnet [16]. This assumption, in particular, implied that the source of magnetism should be located in the center of Earth.

The next major step was made at the beginning of the 19th century, which was marked by a number of discoveries in electromagnetism (Faraday's experiments, the connection between electricity and magnetism, and so on), which by the middle of the century led to the appearance of several competing theories and approaches to describing EMF [17]. The most viable was the approach of Gauss, who used mathematical tools to decompose the magnetic field potential into spherical harmonics:

$$V(r,\theta,\phi)=a\sum_{n,m}(g_n^m\cos m\phi+h_n^m\sin m\phi)\left(\frac{a}{r}\right)^{n+1}P_n^m(\cos\theta)+a\sum_{n,m}(G_n^m\cos m\phi+H_n^m\sin m\phi)\left(\frac{r}{a}\right)^{n+1}P_n^m(\cos\theta)\,. \quad (1)$$

In this expression, the first term is responsible for the field component from sources located inside Earth (i.e., under its surface), and the second is responsible for the field component from external sources (located above the surface). The next qualitative step towards understanding the nature of terrestrial magnetism was the geodynamo mechanism proposed by Walter Elsasser in 1939; the geodynamo is currently the leading theory of the origin of the main EMF component [18]. For a more detailed and complete familiarization with the history of terrestrial magnetism studies, from the first observations to the present day, we refer the reader to [19].

1.2 Modern ideas about Earth's magnetic field

Currently, much is known about EMF: its regular measurements are carried out both in outer space (the Swarm satellite constellation in near-Earth space and the Geotail, Cluster, and Themis satellites in the distant magnetosphere) and on the ground (geomagnetic observatories); geomagnetic surveys (aerial, marine, and others) are also conducted. Data from existing and already decommissioned magnetometers are freely available and can be used by various scientific groups. All this has led to a wide variety of EMF models, distinguished by a wide range of approaches, both software and mathematical.

Earth's magnetosphere can be divided into inner and outer regions, which have no strict boundary but manifest a difference in terms of the applicability of Gauss's approach to describing fields in these regions. Most magnetic field sources in the inner region (especially those generating the dominant component, called the main field) are located outside its boundaries, which allows considering the field to be potential and representing it in the form of a decomposition into spherical harmonics. The magnetic field in the outer region is generated primarily by spatial magnetospheric currents. They fill that region, and therefore the field cannot be considered curl-free there and cannot as a result be described by Eqn (2) below. Building models for these two domains addresses different problems to be solved and involves different principles, experimental data sets, mathematical tools, and other aspects. In this review, we focus on modeling the field in the inner magnetosphere; for the field in the outer magnetosphere, we refer the reader, for example, to [20].

The inner magnetosphere is primarily distinguished by a large number of sources of various natures: from internal currents in Earth's core (Section 2.1) and magnetization of rocks to ionospheric and magnetospheric currents. The magnetic fields generated by them are studied as individual components that make up the total field in the region under consideration. Each such component has different properties, characteristic scales of its features, and different temporal dynamics. However, the same principle is used to describe them: the field is represented as the gradient of the magnetic potential,

$$B=-\nabla V\,, \quad (2)$$

and the magnetic potential is in turn decomposed into spherical harmonics in accordance with (1).

The main difference in describing field components originating in different sources lies in how the decomposition coefficients are found.

Almost all EMF models in the inner magnetosphere primarily describe the main field (the main component of the field in near-Earth space, generated by currents in the liquid core) and/or its variations. The second important component is the lithospheric field. In practice, both components are often described by a single expression for the magnetic potential. Other field components are often considered secondary. This applies, first of all, to the external field generated by magnetospheric currents. In general, it is nonpotential and its standard description (e.g., in Tsyganenko's models [20]) is more involved, but, in this case, importantly, it can also be represented in form (1), (2), because the sources of the component in question are located outside the inner magnetosphere. Individual sources (the ionospheric and associated induced fields, and the tidal field) can be an independent object of study.

The magnetic field configuration reconstructed in the vicinity of Earth can be extrapolated into the interior, to the mantle–core interface. The field values in this region allow reconstructing the dynamics of motion (flows) of a metallic conducting liquid on the surface of the core. There is a class of models in which these flows are used to predict secular variations in the main field, study the geodynamo mechanism, and so on. But numerical approaches to the geodynamo studies are beyond the scope of this review; we refer the interested reader, for instance, to [21].

2. Magnetic field sources and their parameterization

As we have noted, the magnetic field observed near Earth's surface and close to it in the near-Earth space is a superposition of fields from various internal and external sources. The internal sources include 1) currents in the liquid core, 2) lithospheric magnetized rocks, and 3) currents associated with water circulation in the World Ocean. External sources include a system of magnetospheric currents. Ionospheric currents fall into the categories of both internal and external sources, depending on the location of measurements. In addition, the rapidly changing component of the internal magnetospheric and ionospheric fields induces currents in the lithosphere magma and the water of the World Ocean, which in turn generate a secondary field, called the induced field.

2.1 Main field

2.1.1 Source. The main field is generated by currents in the liquid core formed by convective flows of the magnetized liquid, which twist into spirals under the effect of the Coriolis force, forming vortices of different scales. The permanent, undamped generation of a magnetic field in such a system is supported by the geodynamo mechanism (see review [22] and the references therein). In Fig. 1, we schematically show the

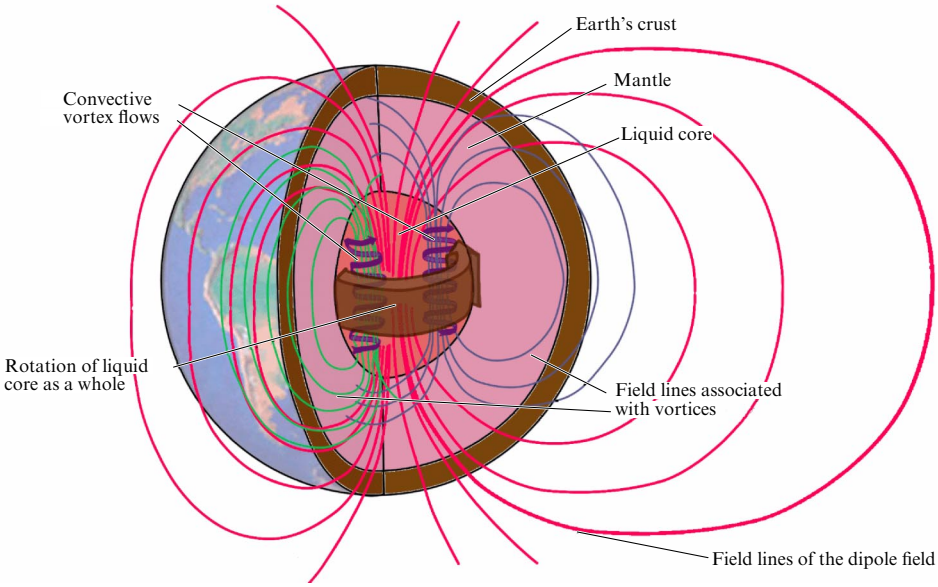

Figure 1. Main field generation scheme.

field generation process. The brown arrow shows the rotation of the liquid core as a whole, responsible for the generation of the dipole component of the field (to be explained below), which is shown with red lines. Dark blue spirals indicate the convective flows generating smaller-scale components of the main field (blue and green lines). The main field is the sum of all such components.

The main field is the dominant component of the magnetic field observed in near-Earth space. On Earth's surface, its contribution is given by more than 95%, ranging from 20,000 nT at the equator to 70,000 nT in the polar regions. It gradually decreases with distance from Earth; at a distance of 8 to 10 Earth radii, it equalizes with the contribution of the component generated by magnetospheric currents.

2.1.2 Parameterization. The potential of the main field is decomposed into spherical harmonics according to Gauss's classical scheme (Eqn (1) without the second term for the external field) and can be found in the literature in two representations:

$$V_i(t,r,\theta,\phi) = a\sum_{n=1}^{N_{\max}}\sum_{m=0}^{n}\left(g_n^m\cos m\phi + h_n^m\sin m\phi\right) \times\left(\frac{a}{r}\right)^{n+1} P_n^m(\cos\theta)\,, \tag{3}$$

$$V_i(t,r,\theta,\phi) = a\sum_{n=1}^{N_{\max}}\sum_{m=0}^{n}\left(\frac{a}{r}\right)^{n+1}\gamma_n^m\,Y_n^m\,(\theta,\phi)\,, \tag{4}$$

where $Y_n^m(\theta,\phi) = P_n^m(\cos\theta)\exp(\mathrm{i}m\phi)$ are spherical functions; $\gamma_n^m = g_n^m - \mathrm{i}h_n^m$; a, r, θ, and ϕ are the characteristic distance, radius, geodetic colatitude, and longitude; n and m are the degree and order of the expansion; g_n^m and h_n^m are the Gauss coefficients expressed in magnetic induction units; P_n^m are the associated Legendre polynomials with Schmidt's normalization; and $N_{\max}$ is the maximum order of the expansion.

The Gauss coefficients g_n^m and h_n^m are fixed in the process of approximating data from experimental studies of the magnetic field. The coefficients at low degrees and orders describe the large-scale structure of the field, and the higher-order ones describe small-scale structures. The relation between a characteristic wavelength that describes the scale of inhomogeneities and the expansion order is given by $\lambda = 2\pi a/\sqrt{n(n+1)}$. The largest-scale structure of the field is formed under the effect of the rotation of Earth (and, accordingly, its liquid core) as a single whole. It is characterized by first-order Gauss coefficients, with g_1^0 determining Earth's dipole moment $M = (4\pi/\mu_0)a^3 g_1^0$; taken together, they determine the angle between the dipole axis and Earth's rotation axis as $\alpha = \arctan\left(\left[(g_1^1)^2 + (h_1^1)^2\right]^{1/2} g_1^0\right)$. The field structure of smaller scales is formed by vortices of a conducting metallic liquid in the core, and the characteristic scale of field inhomogeneities correlates with the vortex size.

2.1.3 Temporal dynamics. The liquid core is a highly dynamical system: the vortices in it undergo constant variations that are stochastic in nature. Changes in the flows in the core are followed by stochastic changes in the configuration of the main field [23]. Such changes are called secular variations of the main field. The most conspicuous manifestations of secular variations include a recent gradual decrease in Earth's magnetic dipole [24]; the motion of Earth's magnetic poles with a periodicity of tens to hundreds of thousands of years, leading to polarity reversals [25]; displacement of the South Atlantic magnetic anomaly [26–28]; and geomagnetic jerks [29]. The term 'secular variation' can be applied to both variations in the Gauss coefficients and changes in field values at specific points, for example, during measurements at specific geomagnetic observatories. As regards variations in the Gauss coefficients, the concept of secular variation coefficients is introduced: these are defined as the time derivatives

$$\frac{\mathrm{d}g_i^j}{\mathrm{d}t} \quad \text{and} \quad \frac{\mathrm{d}h_i^j}{\mathrm{d}t}\,.$$

Secular variations necessitate continuous global measurements of EMF and require parameterizing models not only in space but also in time. The stochastic nature of variations

makes such a problem nontrivial, which gives rise to different proposed solutions, to be discussed in more detail in what follows.

2.1.4 Flows in the liquid core and their relation to secular variations. A natural inner boundary for describing the main field as the gradient of a potential is the core–mantle boundary, which in essence can be regarded as the surface of a source. Field values at this boundary, calculated within the main field models, are the starting point for measuring conductive fluid fluxes in the core. The relation between variations in the main field B at the core–mantle boundary and the core fluxes u is described by the induction equation

$$\frac{\partial B_r}{\partial t} = -\nabla_{\dot{H}}(\mathbf{u}B_r) + \frac{\eta}{r}\nabla^2(rB_r)\,, \tag{5}$$

where η is Earth's magnetic diffusion coefficient, B_r is the radial component of the field vector on the surface of the core, and $\nabla_{\dot{H}}$ is the horizontal gradient operator.

The first term on the right side of (5) describes the advection of fluxes, and the second term describes diffusion. It is believed, however, that the contribution of diffusion to the secular variation is insignificant. In addition, it is quite complicated to derive the model of fluxes **u** from the model for the field B using (5), and therefore the diffusion term is ignored in most cases. This assumption is called the frozen flux approximation [30, 31]. At the same time, taking into account that only the radial component of the field is continuous at the boundary [32], one can replace **u** with its tangential component $\mathbf{u}_h$, which reduces Eqn (5) to

$$\frac{\partial B_r}{\partial t} = -\nabla_{\dot{H}}(\mathbf{u}_h B_r)\,. \tag{6}$$

This assumption is not used in more complex models that describe the geodynamo mechanism numerically. However, such models are beyond the scope of this review.

The set of values of **u** on the entire surface of the core can be represented as a vector field **U**. This representation allows describing the structure of the core and identifying components of different scales, and also provides yet another tool for modeling the main field and its secular variation.

The velocity field **u** is usually considered in a toroidal coordinate system, where it can be decomposed into toroidal and poloidal components T and S [33],

$$\mathbf{u} = \mathbf{u}_{tor} + \mathbf{u}_{pol} = \nabla_{\dot{H}} \times (\hat{\mathbf{r}}T) + \nabla_{\dot{H}}(S)\,, \tag{7}$$

where $\hat{\mathbf{r}}$ is a unit-length radius vector. These components in turn decompose into spherical harmonics:

$$T = \sum_{n=1}^{N_{max}} \sum_{m=0}^{n} \tau_n^m(t)\, Y_n^m(\theta,\phi)\,, \tag{8}$$

$$S = \sum_{n=1}^{N_{max}} \sum_{m=0}^{n} \sigma_n^m(t)\, Y_n^m(\theta,\phi)\,. \tag{9}$$

Expressions (7)–(9) allow describing the spatial and temporal structures of the liquid core, with the τ and σ coefficients at different degrees describing vortices and other structures formed by fluxes of different scales.

It is also worth mentioning the so-called hidden field: a small-scale component of the main field described by harmonics of higher degrees ($n > 13$), identifying which is impossible in ground-based measurements because of the insufficient resolution. In the depths of Earth at the core–mantle boundary, however, the strength of the small-scale component is noticeably higher, and it hence interacts with fluxes in the liquid core, including medium-scale ones. Their variations are in turn responsible for the secular variation coefficients of the corresponding degrees. Calculations show that such a hidden field leads to the majority of spatial errors in calculating the secular variation coefficients [34]. In [35], in particular, the ensemble method was used to show that the main field coefficients up to $n = 40$ can contribute to the secular variation coefficients with $n \leqslant 13$.

2.2 Lithospheric field

2.2.1 Sources. The lithospheric field amounts to approximately 3% of the total field on Earth's surface (although it can reach 8000 nT in some cases) and attenuates with altitude, especially for higher-order harmonics. The source of the lithospheric field is the ferromagnetic rocks of Earth's crust and upper layers of the mantle (asthenosphere), mainly titanomagnetites and titanohematites. Such rocks are magnetized under the effect of an external magnetic field and thus generate their own magnetic field (details about the magnetization of rocks can be found in [36]). The region of the lithosphere where this process is possible is limited by the so-called Curie depth, i.e., the depth where the temperature reaches a critical Curie temperature at which the thermal motion of molecules of the rock substance overcomes the magnetization effect. It is believed that this boundary is located at a depth of up to 24 km in the continental crust and 6 to 7 km in the oceanic crust.

There are two types of magnetization: induced and residual. The induced one (not to be confused with the induced field from external sources; see Section 2.4) arises due to the ordering of magnetic moments in ferromagnetic rock under the effect of the present-day field. Residual magnetization is formed at the instant of cooling the rock and preserves the orientation of the external field as it was at the instant it passed through the Curie temperature. The field caused by the second type of magnetization in most cases prevails over the field of the first type.

In Fig. 2, we show a diagram of the lithospheric field generation. The pink lines show the external field, whose direction determines the alignment of the magnetic moments of ferromagnetic rocks in Earth's crust, shown with parallel black arrows. Also shown are rocks with residual magnetization, whose magnetic moments are not necessarily parallel to present-day external field lines. The lithospheric field is shown with green lines.

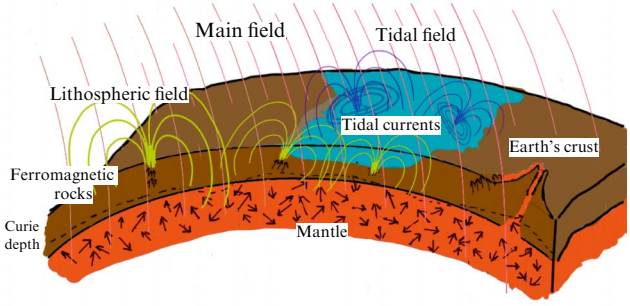

Figure 2. Diagram of the generation of lithospheric and tidal fields.

2.2.2 Parameterization and separation of the main and lithospheric fields. The magnetic potential of the lithospheric field is typically parameterized together with the potential of the main field; the total potential is then also described by expression (3). The reasons for this unified treatment are explained below. In this framework, the main field makes the main contribution to lower-degree harmonics, and the lithospheric field, to higher-degree harmonics. To separate these two components, a spatial power spectrum is constructed, also called the Lowes spectrum [37], which expresses the dependence of R_n on the harmonic degree n:

$$R_n = (n+1)\left(\frac{a}{r}\right)^{2n+4} \sum_{m=0}^{n} \left[(g_n^m)^2 + (h_n^m)^2\right]. \qquad (10)$$

Here, R_n is the energy of the magnetic field of all harmonics of degree n.

In Fig. 3, we show the results of calculations of the Lowes spectrum based on the Gauss coefficients through the 185th order of expansion, taken as an example from the CHAOS-7 model (see Table) for different altitudes. In the range of lower harmonics, the leading contribution to R_n is made by the main field, and in the range of higher harmonics, by the lithospheric field. The transition occurs in the range of the 12th to 20th harmonics, where a break is observed in the graph. A specific boundary inside that range is set differently within different models, depending on their tasks and features.

This behavior of the spectrum, however, does not imply that the lithospheric field makes no contribution to lower-degree harmonics and, most importantly, higher-order ones. In practice, this means that the contribution of the lithospheric field cannot be identified on the background of the main field for small n, and vice versa for $n \gg 20$. In the break region, the contributions of both components are comparable.

It is clear from the figure that the nature of the decrease in R_n with an increase in the degree of harmonics is different for the main and lithospheric fields, depending on the altitude r.

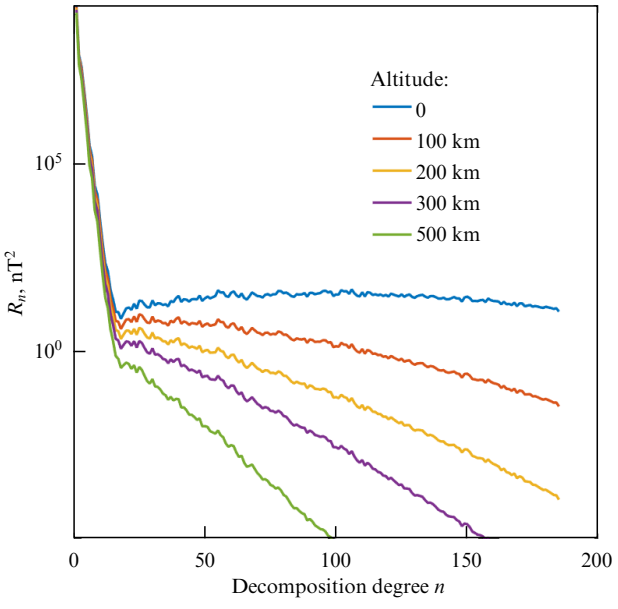

Figure 3. Lowes spectrum at different altitudes, plotted using the coefficients of the CHAOS-7 model for 2021.

For the main field, the slope of the spectrum weakly depends on r, while, for the lithospheric field, the spectrum becomes steeper as r increases.

The upper bound for the degree of expansion of the lithospheric field is limited only by the density of measurements that can be carried out on a global scale on Earth's surface. We mean the spatial density of points of measurement carried out both in geomagnetic observatories and using magnetic surveys. Thus, the highest degree of expansion proposed by the BGS model (see Table) reaches 1440, which corresponds to a wavelength ~ 30 km. In measurements in near-Earth space, the resolvable harmonics extend to the orders 130–140.

2.3 External field

2.3.1 Sources. The external field is generated by spatial currents of Earth's outer magnetosphere. The system of magnetospheric currents includes the ring current, magnetopause currents, magnetotail currents, field-aligned currents, and other currents that arise during magnetospheric disturbances. Most of these currents are schematically shown in Fig. 4.

The ring current consists of particles trapped in the radiation belts, making a longitudinal drift around the planet. It occupies space in the equator region at a distance of 3 to 8 Earth radii and contributes to the magnetic field component parallel to the magnetic dipole axis, weakening it in the region of the magnetic equator and strengthening at the poles. The magnetopause currents (also called Chapman–Ferraro currents) are formed by charged solar wind particles flowing around the magnetosphere; they bound EMF, preventing its field lines from escaping into interplanetary space. The magnetotail currents frame its tail in pairs from the north and the south, closing on the plasma layer and stretching the magnetopause on the night side of Earth. Field-aligned currents (also known as Birkeland currents) flow in a similar way, but close on the polar part of Earth's ionosphere, connecting there with auroral ionospheric currents. On Earth's surface, the corresponding field component contributes no more than 2 to 3%, but it increases with distance. A detailed description of the system of magnetospheric currents can be found, for example, in review [38].

2.3.2 Temporal dynamics. Among the components of the total field, the magnetic fields generated by the currents described above are the ones most exposed to different variations, both

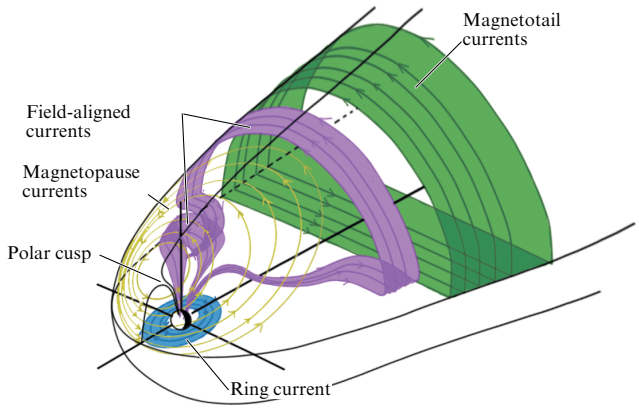

Figure 4. System of magnetospheric currents.

periodic (on the scale of hours, days, and years) and sporadic. Long-period oscillations associated with solar activity cycles and sporadic oscillations associated with solar events arise as a result of the interaction of the solar wind with the magnetosphere. This interaction determines the dayside position of the magnetopause, thereby governing the large-scale structure of currents. The higher the dynamical pressure of the solar wind, the closer to Earth the magnetopause shifts, the more the magnetosphere compresses, and the higher the density of magnetospheric currents (and hence the magnitude of the magnetic fields generated by them). The position of the magnetopause and the structure of currents also depend on other quantities characterizing the solar wind and the interplanetary magnetic field, such as the solar wind speed, its density, the external magnetic field strength vector B, and its vertical component in GSE coordinates. All these quantities fluctuate and correlate with the solar activity cycle, in turn causing magnetopause oscillations, on average within 9 to 11 Earth radii R_E (see Fig. 2 in [39]).

Sporadic events on the Sun, such as coronal mass ejections (CMEs) or corotating interaction regions (CIRs), can increase the speed, density, and dynamical pressure of the solar wind locally in time and space. At such moments, it can compress the magnetosphere to $6.5R_E$ on the dayside. Such rapid intense effects lead not only to a redistribution of existing currents but also to the generation of new ones, characteristic only of periods of such magnetospheric disturbances.

Diurnal and seasonal fluctuations are associated mainly with the rotation of Earth about its axis and around the Sun; among the magnetospheric currents, they mainly affect field-aligned ones, which close on Earth's ionosphere in the polar regions. Seasonal field fluctuations are associated with corresponding seasonal fluctuations in the electrical conductivity of the ionosphere, which depends on the intensity of ultraviolet radiation interacting with the upper layers of the atmosphere, whereas daily fluctuations are associated with the fact that geomagnetic poles do not coincide with the geographical ones and rotate around them [40].

2.3.3 Parameterization. In decomposing the external field into spherical harmonics in accordance with (1), only the second term is preserved there, because only the contribution of the external field to measurements carried out on Earth's surface and in the area of operation of low-orbit satellites is important in developing EMF models, and the field under consideration is external with respect to such measurements. The main feature here is the large-scale nature of the external field, which determines the use of the lowest degrees and orders, typically up to 1 or 2. In addition, due to spatial heterogeneity and complex time behavior, the magnetic potential is often divided into components in accordance with different spatial and temporary characteristics. This gives rise to a wide variety of models.

In the CHAOS model (see Table), the potential is decomposed into two components corresponding to nearby magnetospheric sources (ring and field-aligned currents),

$$V_{SM} = a\sum_{m=0}^{1}\left[q_1^{m,SM}(t)\cos mT_d + s_1^{m,SM}(t)\sin mT_d\right] \times \left(\frac{r}{a}\right)P_1^m(\cos\theta_d) + \dots, \quad (11)$$

and distant ones (magnetotail and magnetopause currents),

$$V_{GSM} = a\sum_{n=1}^{2} q_n^{0,GSM} R_n^{0,GSM}(t, r, \theta, \phi). \quad (12)$$

In these expressions, the subscripts SM and GSM reflect the fact that the breakdowns are carried out in the respective Solar Magnetic and Geocentric Solar Magnetospheric coordinate systems; T_d and θ_d are the dipole local time and the dipole colatitude, and $R_n^{0,GSM}$ is a modification of spherical harmonics in the GSM system. The expression for V_{SM} is actually somewhat more complicated than the one presented here, and includes terms describing long-term variations as well as separately described harmonics of the second degree of decomposition (see Eqns (2a)–(2c) in [27]).

Another option is to divide the field into components in accordance with the nature of time dynamics. In the BGS model (see Table), the potential is thus decomposed into three components, V_{ext}, V_{ann}, and V_{VMD}, given by [41]

$$V_{ext}(t, r, \theta, \phi) = a\sum_{m=-1}^{+1} q_1^m(t)\, Y_1^m(\theta, \phi), \quad (13)$$

$$V_{ann}(t, r, \theta, \phi, \tilde{\phi}) = a\sum_{m=-1}^{+1}\left[e_1^m(t)\left(\frac{r}{a}\right) + \imath_1^m(t)\left(\frac{a}{r}\right)^2\right]Y_1^m(\theta, \phi) + a\sum_{m=-1}^{+1}\epsilon_1^m(t)\left(\frac{r}{a}\right)Y_1^m(\theta, \tilde{\phi}), \quad (14)$$

$$V_{VMD}(t, r, \theta, \phi, VMD) = a\sum_{m=-1}^{+1}\left\{b_1^m(t)\, VMD_{ext}^m\left(\frac{r}{a}\right) + c_1^m(t) VMD_{int}^m(t)\left(\frac{a}{r}\right)^2\right\}Y_1^m(\theta, \phi). \quad (15)$$

Here, V_{ext} is the component characterizing long-term variations on a scale of several years; the coefficients q_1^m are calculated experimentally with a frequency of once every few months and are interpolated by B-splines; V_{ann} describes the potential of a component experiencing regular variations with a period of one year, six months, and one day. In (14), the coefficients in square brackets describe the actual external field component $\imath_1^m(t)$ characterized by annual and semi-annual variations, and its internal induced part $e_1^m(t)$, whose nature is described in detail in Section 2.5. The component with a characteristic period of variations given by one day is described by the second term with the coefficients $\epsilon_1^m(t)$ (here, instead of the geodetic longitude, the Sun-synchronous longitude $\tilde{\phi}$ is used). Finally, the term V_{VMD} describes variations associated with magnetospheric disturbances, which in this case are described by the magnetospheric index VMD. It is worth noting that most models work under conditions of a quiet magnetosphere, which means that the terms describing the dependence of the potential on magnetospheric indices are defined within narrow limits corresponding to a quiet magnetosphere.

In other versions, the external field potential is expressed by a single term of the form (13), but the coefficients are calculated with a very high cadence (for example, once per

hour) and are then interpolated. An example here is provided by the CM (Comprehensive Model) or COV-OBS models (see Table). It is actually difficult to find any comparative analysis of different approaches to parameterizing the external field in EMF models in the literature, and the choice of a particular approach is largely determined by personal preferences of the authors of the models.

Worthy of special note are so-called toroidal fields, which are also parameterized in certain older versions of the CM [42] and GRIMM [43] models. Such fields are generated by field-aligned currents at altitudes of 400 to 700 km in polar latitudes, also called the F-region. But they are typically not included in modern models.

2.4 Ionospheric field

2.4.1 Sources. The source of the ionospheric field is ionospheric currents flowing in the so-called conducting E-layer at altitudes of 90 to 150 km. They are associated with the circulation of air masses in the neutral atmosphere, the atmospheric tides, which are in turn caused by heating of the atmosphere by the Sun, the Moon's gravity, and other factors. The waves of these oscillations reach the ionosphere, acting asymmetrically on ions and electrons: they cause the motion of only the former. This is because the cyclotron frequency of ions is less than or comparable to the frequency of their collisions with the neutral-atmosphere atoms as an atmospheric wave propagates, while the corresponding cyclotron frequency for electrons is much higher and atmospheric waves do not induce their motion.

The system of ionospheric currents in magnetically quiet conditions includes quiet time currents (Sq) circulating in temperate latitudes on the dayside, the equatorial electrojet (EEJ) formed by charged particles moving eastward exactly above the geomagnetic equator, auroral electrojets located in pairs in the polar regions, and other currents. The current system is shown in Fig. 5. During magnetospheric disturbances, Sq currents are superseded by Sd currents of the disturbed ionosphere.

The average contribution of the ionospheric field is of the order of tens of nT; a local contribution can be much larger, especially in polar latitudes, becoming dominant and reaching thousands of nT during magnetospheric disturbances.

2.4.2 Temporal dynamics. As in the case of currents in the near magnetosphere, the dynamics of ionospheric currents are influenced by seasonal variations in the electrical conductivity of the ionosphere. Another important source of variation is tidal cycles, the main ones being the 24-hour cycle associated with the heating of the atmosphere and the 12-hour cycle associated with the motion of the Moon and its gravitational effect on Earth's atmosphere. There are also cycles with characteristic periods of 8 and 6 hours. A detailed description of ionospheric currents and their variations can be found in review [44].

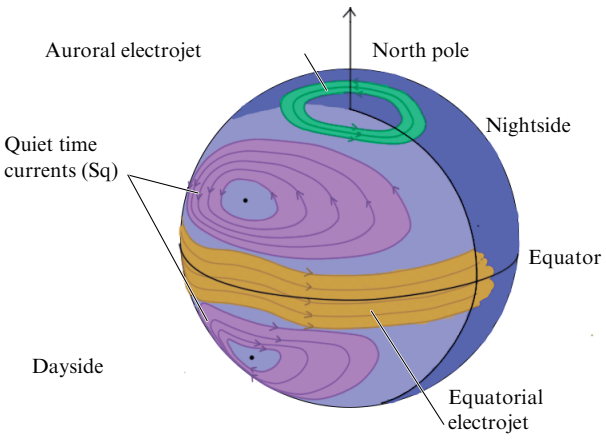

Figure 5. System of ionospheric currents.

2.4.3 Parameterization. There are very few EMF models that include the ionospheric field, and it is therefore quite difficult to speak about the generally accepted approaches to its parameterization. However, its key features can be identified. First, the ionospheric field is one of the most difficult to parameterize in terms of spherical harmonics: because the currents are close to the field measurement region, describing their configuration requires a decomposition into harmonics of quite high degrees. In modern models, e.g., Kalmag (see Table), this value reaches 50. Second, the currents and hence the field exhibit an extremely complex behavior in time with the amplitude of variations generally comparable to the value of the field itself, which does not allow ignoring them. To describe this behavior in the CM model (see Table), the magnetic potential is decomposed into a large number of components corresponding to different oscillation periods. Short-period modes (with the 24′, 12′, 8′, and 6-hour periods) and long-period (annual and semi-annual) ones are separated such that each component describes a particular combination of a long-period and a short-period mode. In addition, each of these potentials is preliminarily decomposed into spherical harmonics in a quasidipole coordinate system tied to EMF. The total magnetic potential of the ionospheric field is therefore written in the form of several nested sums,

$$V_{\rm ion}(t,\mathbf{r}) = \sum_{s=-2}^{+2}\sum_{p=0}^{4}\sum_{l=p-1}^{p+1}\sum_{k=\max(1,|l|)}^{|l|+40} \tilde{\epsilon}^{\,l}_{ksp} V^{kp}_{sp}(t,\mathbf{r})\,, \qquad (16)$$

where the potential for the area below and above the source is described by the respective expressions

$$V^{kp}_{sp} = \mathrm{Re}\left\{ a \sum_{n=1}^{60} \sum_{m=-\min(n,12)}^{\min(n,12)} \left[\left(d^{lm}_{kn,e}\right)^* \left(\frac{r}{a}\right)^n + \left(f^{lm}_{knsp}\right)^* \left(\frac{a}{r}\right)^{n+1} \right] P^m_n(\cos\theta_d) \times \right.$$
$$\left. \times \exp\left(\mathrm{i}(m\phi_d + \omega_s s t) + \omega_p p t_{mut}\right) \right\}, \qquad (17)$$

and

$$V^{kp}_{sp} = \mathrm{Re}\left\{ a \sum_{n=1}^{60} \sum_{m=-\min(n,12)}^{\min(n,12)} \left[\left(z^{lm}_{kn}\right)^* + \left(f^{lm}_{knsp}\right)^* \right] \times \left(\frac{a}{r}\right)^{n+1} P^m_n(\cos\theta_d) \exp\left[\mathrm{i}(m\phi_d + \omega_s s t) + \omega_p p t_{mut}\right] \right\}. \qquad (18)$$

Here, a is Earth's radius; $\tilde{\epsilon}^{\,l}_{ksp}$ are the coefficients depending on the solar activity level; $d^{lm}_{kn,e}$ and z^{lm}_{kn} describe the field potential from the ionospheric currents proper, and f^{lm}_{knsp}, from currents induced by them in Earth's mantle; $p = 1, 2, 3, 4$ characterizes short-period modes corresponding to 24, 12, 8, and 6 hours; s are long-period modes; ω_s is the fundamental seasonal angular frequency, equal to

2π rad year^{-1}; and ω_p is the fundamental daily angular frequency equal to $2\pi/24$ rad h^{-1}. A more detailed description can be found in Eqns (7)–(26) in [45].

2.5 Induced fields

2.5.1 Sources. Induced fields are generated by currents arising in the conducting medium of the world's oceans and Earth's mantle under the influence of field components external to them that vary over time. The sources of such an external field are primarily the currents of the ionosphere and nearby sources of the external magnetosphere (ring and field-aligned currents). The characteristics of induced currents (and hence of the fields they generate) depend primarily on the electrical conductivity of the medium, the frequency of the inducing field, and its scale. The highest specific electrical conductivity is here exhibited by ocean water [46] and also deep (> 1000 km) layers of the mantle, where it reaches values of ~ 2–3 S m^{-1}. The electrical conductivity of the mantle decreases with decreasing depth (see, e.g., Fig. 2 in [47]). The continental crust has minimal conductivity values and is least susceptible to the influence of inducing fields. The oscillation period of the inducing field is the second main factor influencing the magnitude of the induced field. For example, oscillations with a period of the order of several minutes lead to an induced field that practically coincides with the inducing one, while oscillations with a period of a day generate a field several times weaker. Regarding the size of the source field, its large-scale components induce more intense currents (and therefore fields) than the small-scale ones do.

This dependence manifests itself, for example, in the fact that the induced component from the average-scale ionospheric quiet time currents (Sq) reaches one third of the corresponding ionospheric field on Earth's surface, while the same component from the equatorial electrojet with the characteristic small-scale structure of its field does not exceed 15% (see Fig. 10 in [47]).

Among other important features of induced fields, it is worth noting that oscillations in the induced field repeat oscillations in the corresponding inducing one with a slight delay.

2.5.2 Parameterization. The potential of the induced field decomposes into spherical harmonics in the same way as the inducing one does. Moreover, because it is extremely difficult to identify its signal in real measurements, it is calculated in practice based on the characteristics of the corresponding source field. The point is that each harmonic $\{m,n\}$ of the inducing field potential can be associated with the corresponding harmonic $\{k,l\}$ of the induced field potential. We then say that the $\{m,n\}$ harmonic of the inducing field generates the $\{k,l\}$ harmonic of the induced field. This relation is expressed by the dependence of the Gauss coefficients ϵ_n^m of the induced field on the coefficients $\imath_k^l$ of the inducing field via a convolution with the transfer function $Q_{kn}^{lm}(\omega,\sigma)$, which includes the oscillation frequency of the inducing field ω and the electrical conductivity of the medium σ. In general, each harmonic of the induced field generates all possible harmonics of the induced field, and the corresponding coefficients are calculated as

$$\imath_k^l(\omega,\sigma) = \sum_{n=1}^{N}\sum_{m=-n}^{n} Q_{kn}^{lm}(\omega,\sigma)\,\epsilon_n^m(\omega)\,. \tag{19}$$

To calculate the transfer function, Earth conductivity models are used. Modern models include a three-dimensional model for Earth's mantle and a one-dimensional model for the World Ocean [48, 49]. However, it is often sufficient to use a totally one-dimensional model (i.e., one where the electrical conductivity depends only on depth); in that approximation, each harmonic of the inducing field generates only one corresponding harmonic of the induced one, and Q_{kn}^{lm} is then a diagonal matrix.

Another difficulty is that the time dynamics of real fields are too complex to be described by an oscillation with a single frequency ω. Therefore, in practice, the signal is decomposed into harmonics over time, its leading frequencies are identified, and the induced field potential coefficients are calculated for each frequency separately. For example, in calculating induced fields in the CHAOS model (see Table), frequencies with a period from one hour to four years are selected via the Fourier analysis.

It is therefore reasonable that, under such conditions, the induced field is parameterized together with the inducing one, as we can see in Eqns (14) and (18). The coefficients $q_1^{m,\mathrm{SM}}$ and $s_1^{m,\mathrm{SM}}$ in Eqn (11) are combinations of the coefficients ϵ and $\imath$,

$$q_1^{m,\mathrm{SM}} = \hat{q}_1^m\left[\epsilon(t) + \imath\left(\frac{a}{r}\right)^3\right], \tag{20}$$

$$s_1^{m,\mathrm{SM}} = \hat{s}_1^m\left[\epsilon(t) + \imath\left(\frac{a}{r}\right)^3\right], \tag{21}$$

where ϵ and $\imath$ are the respective Gauss coefficients for the external field and the field induced by it, and $\hat{q}_1^m$ is a static regression coefficient.

2.6 Tidal field

Tidal magnetic fields are created by currents induced by masses of water in the World Ocean moving cyclically under the influence of tidal forces in Earth's external magnetic field. The generation of such fields is shown in Fig. 2. Blue concentric lines show the direction of water circulation in the external magnetic field, which is the sum of the main field (pink lines) and the lithospheric field (green lines). The blue lines show the tidal field lines.

The magnitude of a field induced in this way depends on the period and amplitude of oscillations of water in the World Ocean. Oscillations are decomposed into several components corresponding to different physical processes: the rotation of the Moon around Earth, Earth's rotation about its axis and around the Sun, nutation of Earth's axis and of the Moon's orbit, variations in the distance to the Moon, and many others. Modern measurement accuracy allows identifying more than 400 components, but, for example, only about 60 are used to calculate tidal heights. The most significant are the semidiurnal components M2, N2, and S2 and the diurnal ones N1 and O1. The tidal fields considered are associated with these individual components. The M2 component induces the strongest field, reaching 5–6 nT on Earth's surface and 2–3 nT at the altitudes of low-orbit satellites. The N2 and O1 components are respectively of the order of 0.5 and 0.1 nT. The signal from the other components is already quite difficult to identify in experimental data. Tidal fields are classified as large-scale ones and have their maximum at $n = 3$–6 on the corresponding Lowes spectrum for the M2, N2, and O1 components (see Fig. 5 in [50]).

2.6.1 Parameterization. Currently, the tidal field is considered, among other sources, in only one model, the CM (see Table). In this model, the magnetic potential is considered separately for each of the three components M2, N2, and O1, and time variations are described by a separate term, which includes a frequency ω:

$$V(\Delta t, \mathbf{r}) = \mathrm{Re}\left\{ a \sum_{n=0}^{N_{\max}} \sum_{m=-n}^{n} \left(\frac{a}{r}\right)^{n+1} (\tau_n^m)^* \times P_n^m(\cos\theta) \exp\left[\mathrm{i}(m\phi + \omega\Delta t)\right] \right\}. \quad (22)$$

In addition, there are other fields associated with the motion of water in the World Ocean, for example, fields induced by regular currents [51]. The greatest contribution among such currents is made by the Antarctic circumpolar current, which induces a magnetic field comparable to the tidal one in absolute value. Fields are also induced by tsunami waves, in which, unlike ordinary waves, a longitudinal transfer of water masses occurs [52]. But these components are not considered in magnetic field models and are therefore beyond the scope of this review. More details about the fields induced by the motion of water in the World Ocean can be found in review [53].

3. Experimental data

The main sources of information about the magnetic field are presently measurements made by satellites, at geomagnetic observatories, and within magnetic surveys and expeditions. Each of these sources plays a role in the study of EMF. Satellite data provide the main array for analyzing almost all field components; data from geomagnetic observatories provide measurements of the field on Earth's surface and are also used to calculate geomagnetic activity indices used to select magnetically quiet periods, including in satellite data. Magnetic survey data are used to study the smallest-scale components of the lithospheric field and to build local models and retrospective models, where historical magnetic surveys are the only source of experimental data. In addition, other data can be taken into account to study individual field components. For example, when studying induced and tidal fields, voltage measurements are carried out in deep-sea communication cables [54].

3.1 Historical detour

Historically, the accumulation of data on the magnetic field began with the development of long-distance navigation in the 15th century, associated with the intensive use of the compass. At the same time, sailors began to notice that the direction of the compass needle does not always coincide with the direction to the north and varies from place to place. To make corrections, they made notes on portable sundials, which can be considered a precursor to measurements of magnetic declinations [55]. The first such findings date back to the first half of the 15th century; already a century later, measurements of magnetic declinations became a routine procedure in navigating across seas. The earliest such measurements date back to 1510 (see Fig. 2 in [56]); they were flourishing from the beginning of the 17th century, in particular with the start of the Dutch West India Company in 1621, which opened a period of intense trade and, accordingly, shipping in the Indian and Atlantic oceans. Data from ship logs from this period (up to 1840) constitute a significant proportion of all data that now serve as the basis for building retrospective models of EMF [57]. It is also worth noting that, although the first inclinometer (a device for measuring magnetic inclination, i.e., the angle between the horizontal plane and the direction of the field strength vector) was invented in 1580, it was not of great interest for sea navigation, and therefore the overwhelming majority of data from sea expeditions for this period contain only magnetic declination values.

From the 18th century, due to the growth of scientific interest in the phenomenon of terrestrial magnetism, scientific expeditions began to be sent to measure and map the magnetic field. The first such expedition was Edmund Halley's Atlantic voyage in 1699; since then, maps of magnetic declinations and inclinations have been created by various researchers on a constant basis. The next important milestone was Ross's expedition to search for the South Magnetic Pole, organized in 1839–1843 as part of the so-called magnetic crusade [17], which resulted in creating maps of magnetic declinations and inclinations in the southern hemisphere. In general, since the mid-19th century, when a great leap occurred in both measurement methods and understanding of the nature of electromagnetism, such expeditions have taken the form of marine magnetic surveys, which are regularly carried out to this day. Such historical data are a unique source of information for modeling EMF in that era. To date, a large collection of historical marine geomagnetic measurements has been gathered and digitized by Jonkers [56]; it was used primarily to build the gUFM model (see Table).

Scientific interest also resulted in the creation of a second important source of experimental data, whose importance is preserved to this day: geomagnetic observatories. The first periodic local measurements of the magnetic field began near London in 1540 [58] and near Paris in 1541 [59]. In particular, as a result of observations in London in 1635, the magnetic declination was discovered to change with time. This fact determined the need for constant long-period measurements at a fixed location, which ultimately led to the creation of geomagnetic observatories. However, such measurements were scarce until the beginning of the 19th century.

The first half of the 19th century was marked by a big leap in understanding the nature of electromagnetism, as well as in the technical tools for experiments. During that period, Gauss invented a method for calculating the absolute values of the field strength, independent of the device and the characteristics of the medium; the accuracy and quality of measuring instruments (magnetic theodolites and magnetographs) was noticeably improved. All this provided the fundamental possibility of complete, accurate, and regular measurements of the magnetic field. The first such observations began in London in 1818 (albeit interrupted in 1820), in Paris in 1820, and in Kazan in 1823. Already in 1829, Alexander von Humboldt, to test his theory about the simultaneity of field disturbances in different areas on Earth during magnetic storms, built the first network of geomagnetic observatories, which, in addition to the already mentioned observatories in Paris and Kazan, also included newly built ones in Berlin and Freiburg.

The Russian Empire played an important role at these initial (as well as future) stages, by making a significant contribution to the expansion of this first network. At the time the first Geomagnetic Observatory in Kazan started up, the Russian Empire had already accumulated a wealth of

experience in geomagnetic measurements; in St. Petersburg, for example, periodic measurements began in 1700 [60]. Following the observatory in Kazan headed by A Ya Kupfer, observatories were opened in Crimea, St. Petersburg, and then throughout the Russian Empire up to Nerchinsk in the Transbaikal region (and also in Beijing), which allowed covering vast territories in the northern part of Asia. They immediately became part of the Humboldt network and then of its successor, the Göttingen Magnetic Union, founded in 1836 under the auspices of the Royal Society of London.

Subsequently, in the framework of this union, geomagnetic observatories were built in English colonies around the globe, and by 1842 their number had already reached 50. Global field measurements within this network, notably, allowed Gauss to test his mathematical model of the magnetic field and verify its applicability. Details about this period of the development of geomagnetic measurements can be found in reviews [61] and [62]. Since then, the number of magnetic observatories in the world has steadily increased. In those locations where building them was impractical, repeat stations were arranged, to which equipment was delivered and measurements taken several times a year. The data from such stations, however, had to be calibrated to the readings of the nearest full-fledged observatory.

3.2 Current state

The beginning of the modern era of magnetic field measurements can arguably be set as the period 1940–1950, when a significant technological leap occurred both in methods for measuring magnetic fields (modern types of magnetometers, fluxgate and proton, which were more accurate and easier to use) and in related fields. This allowed mass measurements for a variety of purposes to be started. That period saw the start of continental aeromagnetic surveys and more local ones for mineral exploration. Geomagnetic observatories were equipped with new types of magnetometers, and with the beginning of the space era they were also installed on spacecraft. Their detailed description is left beyond the scope of this paper, because the data from sea, air, and other similar magnetic surveys are typically not used in developing modern EMF models with a small number of harmonics ($n < 20$).

3.2.1 Geomagnetic observatories. Magnetic observatories are currently one of the most important sources of data, primarily on the field variations, ranging from the secular main field variations to those associated with ionospheric and magnetospheric sources with a period of about a minute.

There are currently about 150 observatories in the world that take measurements at minute (and, as of 2016, often second) intervals (the oldest observatories have been taking measurements since the 1820s). They are equipped with vector fluxgate magnetometers that measure individual components of the magnetic field vector. One of the disadvantages of such magnetometers is that they require periodic calibration, because their readings are distorted over time, the sensors tend to degrade, and external conditions can also change, for example, the orientation of the base on which the magnetometer is installed. To calibrate them, absolute measurements with a scalar magnetometer and angular measurements with an inclinometer/declinometer are used at certain intervals to calculate corrections to the readings of the vector magnetometer. The calibration measurement data are then interpolated and smoothed to form a so-called *baseline*, the accuracy of which directly affects the overall accuracy of the observatory data [63]. This procedure is standardized and carried out in each observatory.

Modern geomagnetic observatories are used for different purposes and conduct observations within different organizations (not always scientific ones). Many scientific tasks, including the construction of EMF models, require the greatest possible coverage and simultaneous access to data from all possible measurements. For these purposes, as well as to standardize the measurement process, the INTERMAGNET program was launched in 1987 [64], which sets requirements for the data released, and certifies and coordinates different observatories. Another important organization is the World Data System (WDS), which currently provides near real-time collection and storage of raw data from observatories around the world.

Although observatory data undergo the required internal quality checks and release their average hourly, average monthly, and average annual values of the magnitude and components of the magnetic field vector, even more careful processing is nevertheless required when developing EMF models, for example, for joint analyses with satellite measurement data. Such post-processing began back in 2013 [65] as part of the preparation of the Swarm mission and is ongoing; the data adjusted in this way are posted on the mission website. More details about measurements carried out at magnetic observatories can be found in review [66].

In addition to field measurements, geomagnetic observatories provide a variety of geomagnetic indices that are needed both in selecting experimental data and in building models (for example, some of them are directly used in the parameterization of external fields; see Eqn (15)). Such indices are calculated from readings of several observatories located in a region that is considered most sensitive to disturbances associated with a particular source being measured. For example, the geomagnetic disturbance index K_p is calculated at the Potsdam Center based on readings from 13 observatories located in temperate latitudes. This index reflects all irregular disturbances in the magnetic field caused by the flux of solar wind particles, to which these particular regions are sensitive. The D_{st} index, which describes disturbances associated with variations in the ring current, is calculated by Kyoto University based on data from four observatories located at tropical latitudes. There are also indices linked to measurements in the auroral ellipse (AE), directly in the polar caps (PC), and others. A detailed description of geomagnetic indices can be found in review [67].

3.2.2 Satellite measurements. The beginning of the space age opened up new opportunities for studying the magnetic field. Magnetometers began to be installed on spacecraft almost from the very first flights: the first such stations were the Soviet Sputnik-3 and the American Vanguard-3, and the first spacecraft specifically designed for measuring the magnetic field were the Soviet spacecraft Kosmos-26 and 49 (1964) [68], Kosmos-321 and 356 (1970) [69], and the American series of POGO spacecraft (1965–1971), including satellites OGO-2, 4, and 6 [70]. By that time, installing magnetometers on spacecraft had become widespread. The next step towards increasing the measurement accuracy was the transition to a combination of scalar and vector magnetometers. The former allow measuring the magnitude of the magnetic field with good accuracy, and the latter allow measuring the

direction. In addition, scalar magnetometers are typically used to calibrate vector magnetometers. Although the first spacecraft with such a combination of magnetometers was Magsat [71], which operated from 1979 to 1980, regular use started in 1999 with the Ørsted, SAC-C, and CHAMP experiments.

Field measurements by magnetometers installed on satellites underlie all modern models, because they provide uniform coverage of Earth's entire surface (which is not provided, for example, by geomagnetic observatories, which are prevalent in the northern hemisphere) and allow spatially separating different field sources. Four experiments marked the beginning of the era of high-precision satellite measurements of the magnetic field, which have been operational for more than twenty years: Ørsted, SAC-C (Ørsted-2), CHAMP, and the Swarm constellation of satellites. Each of the experiments followed roughly the same plan: in all cases, the installation includes two types of magnetometers (scalar and vector) mounted on a rod to separate them from the background fields of the spacecraft body. A vector magnetometer (with a fluxgate type of magnetometer typically used for that purpose) is installed in conjunction with a star tracker to obtain the most accurate data possible on the orientation of the magnetometer. In all cases (with the exception of Swarm), the scalar magnetometer is the one whose operating principle is based on the Overhauser effect, which ensures the stability of its characteristics over time. Its main task is to provide calibration of the vector magnetometer, which degrades over time. The above experiments were carried out (and continue to be carried out in the case of Swarm) in low Earth orbit, from 400 to 700 km. The accuracy of measuring the magnetic field components by the devices ranges from 1–2 nT for CHAMP and Swarm to 5 nT for Ørsted and Ørsted-2.

The first of these instruments, the Ørsted microsatellite launched in February 1999, was developed in Denmark exclusively for the purpose of magnetic field mapping [72]. In December 2004, due to the breakdown of the star trackers, the vector data transmitted by the spacecraft lost practical value, and in 2014, despite the operability of all systems, it was decided to stop on-board operations due to the low value of the data in light of the emerging new experiments. The CHAMP (Challenging Minisatellite Payload) minisatellite, developed at the Potsdam Research Center for the study of Earth's gravity and magnetic field and for atmospheric and ionospheric sensing, was launched into orbit in July 2000. Following it, in November 2000, the international mission SAC-C was launched with the Ørsted-2 magnetic field mapping unit [73], similar to Ørsted. This unit, however, produced only scalar data and operated until the end of 2004. CHAMP was scheduled to cease operation in September 2010, having descended to altitudes of < 200 km and provided the lowest orbital magnetic field measurements to date.

In November 2013, the European Space Agency's Swarm mission was launched, consisting of three satellites: Alpha (A), Bravo (B), and Charlie (C) [74]. The Alpha and Charlie spacecraft were launched into permanent low (460 km) subpolar (87.4°) orbits separated by 1.4° in longitude. When moving along the orbits, one satellite lags behind the other by several seconds. Bravo moves in a separate higher (530 km) orbit with a slightly higher inclination (88.0°). The close proximity of the orbits of the first pair of satellites allows measuring the longitudinal field gradient. This makes it easier to solve an important problem in all satellite magnetic field measurements: when the field strength changes during the satellite's motion, it is not known whether it changes in space or time due to the arrival of some magnetospheric disturbance. Such measurements are primarily important when studying the main, lithospheric, and ionospheric fields, i.e., the components that manifest themselves most strongly on the surface of Earth and in its immediate vicinity. That is why such a scheme was implemented for the lower orbital part of the constellation. Slightly different orbital parameters for Bravo mean that its orbit gradually rotates relative to the orbits of Alpha and Charlie. This is important primarily when studying the external field, when simultaneous measurements at points corresponding to different local times are important for reconstructing the spatial picture in quiet times and during disturbances. This also allows distinguishing between seasonal and diurnal variations in the parameters of the external magnetic field.

It is worth noting that data from other space magnetometers are also in demand. For example, to fill the gap between the completion of the CHAMP mission and the launch of the Swarm group, which lasted from 2010 to 2013 (no high-precision vector measurements were made during that period), and in the CHAOS model (see Table), vector measurements on the CryoSat-2 spacecraft were used. This last device does not have a scalar magnetometer, which causes difficulties with vector calibration, which is to be done independently when processing data; the existing EMF models are used for this purpose [75]. Vector measurements were used in the same way on the DE-2 satellite (1981–1983), mainly in older models [76]. In addition, it is worth pointing out the recently launched Chinese–Italian project CSES for research in a number of areas, including EMF monitoring [77, 78]. Recently, data from the Iridium constellation of satellites (together with data from geomagnetic observatories) [79], field measurements on the ISS [80], and other sources are in use when building EMF models.

Data obtained from these and other spacecraft are publicly available on the official website of the Swarm mission [81], on the website of the Technical University of Denmark [82], the CSES mission resource [83], and other resources and are available for use by everyone, which mainly defines the large number of scientific teams working on the creation of EMF models.

3.3 Data selection

Experimental data typically come to model developers already in the form of a finished product (this is especially true for modern satellite experiments and geomagnetic observatories), which have already been preprocessed to exclude uncertain events. Therefore, we deal in this section not with the technical selection of 'good' events in the experimental data but rather with the separation of events associated with different field components and with different magnetospheric phenomena. There are several selection elements, some of which apply to any model (for example, exclusion of magnetospheric disturbances), and some only to models that use a sequential approach, a characteristic feature of which is the exclusion of signals from 'unnecessary' sources from the data. In fact, the main subject of study for most models is the main field (together with the lithospheric field, if the model includes the decomposition of their common potential into harmonics of the corresponding degrees), whose potential is often estimated together with the external potential in modern models. Typically, therefore,

one strives to exclude the signal from the ionospheric and the corresponding induced fields from experimental data. The contribution of other sources is usually disregarded.

Excluding the disturbed magnetosphere periods is an important element in the development of EMF models, because, during such periods, it is quite difficult to calculate the behavior of fields with the required accuracy. For satellite data, such a selection is largely based on the values of geomagnetic indices. The specific indices and parameters used in models vary greatly among the model creators; we note K_p, D_{st}, *RC* (which characterizes the ring current as D_{st} does, but is measured according to data from 21 observatories) [84], and VMD (which describes disturbances of the external and corresponding induced field based on the readings of all INTERMAGNET geomagnetic observatories located on the night side within the $\pm 50^\circ$ geomagnetic latitude) [85]. The reason for such a variety of indices is that none of them is universal and global. Because each index is a combination of data from a separate set of observatories, it rather reflects the local degree of disturbance in the corresponding areas. This state of affairs is a significant problem for further increasing the accuracy of models, as discussed in detail in [86]. In addition to magnetospheric indices, various parameters of the solar wind and interplanetary magnetic field are used to select magnetic quiet time. For example, negative values of the z-component of the interplanetary magnetic field are associated with magnetic storms; at such moments, the interplanetary field changes direction to become opposite to the EMF direction and the magnetic force lines on the day side of the Earth reconnect, moving to the opposite side of the polar cusps, which causes an instant redistribution of energy. Such periods are therefore also excluded from the analysis. In the case of observatories, in addition to a careful analysis of time series, the subtraction of the signal from external sources calculated by external field models is also used for that purpose.

The easiest way to eliminate ionospheric field signals is to exclude measurements on the dayside. Although this is an expensive method from a statistical standpoint, it is used very broadly. Technically, this selection is carried out by limiting the local time or the angle between the direction to the Sun and the horizon. Another way to take the ionospheric component into account is to independently calculate it using third-party models (most often, the CM model) and subtract the result from the measurement results. This procedure is performed both for space measurements and for measurements in observatories.

The polar regions are special in terms of data use. It is no longer possible to say that these areas are free from field sources, because field-aligned currents flow there, connecting the magnetospheric current system with the ionospheric one. Most models only use scalar field measurements in these regions if obtained from satellites, because field-aligned currents are believed to distort the direction of the vector but not the absolute value of the field strength.

Another way to select data is to compare it with that from the existing models. Within this approach, experimental results that differ greatly from model predictions are discarded from the analysis.

3.3.1 Sequential and comprehensive approaches. The strategies to 'process' signals from different field sources and take them into account when developing a model can be divided into two categories: sequential and comprehensive. In the sequential approach, it is assumed, first of all, that the area of interest is some single field component (these are primarily the main and lithospheric fields). With this approach, signals from extraneous components are excluded or subtracted from the experimental data at the selection stage, and then the selected signal of the desired component is estimated. The comprehensive approach emerged as an alternative to the sequential one and is primarily associated with the CM model (see Table), which literally means Comprehensive Model. This approach involves a simultaneous estimation of several field components in order to obtain the form of their potential at once. It is worth noting that the term 'sequential' is not used when describing the models themselves, because this approach is historically standard and implicit.

The current state, however, is such that most models that focus on the main field in one way or another are either comprehensive or incorporate both approaches. A typical algorithm for the model operation is to exclude the signal of the ionospheric component from the experimental data, but at the same time co-estimate the external and main fields (the corresponding induced components are then excluded/estimated in the same way as the inducing ones; for example, if the ionospheric field is excluded from the co-estimation, then the component induced by it is also excluded). In addition to the CM, fully comprehensive models also include the Kalmag model (see Table) and older versions of the GRIMM models [32, 43]. The separation between these approaches appears to be somewhat more explicit in creating models of only the lithospheric field, where the sought-after field is not dominant among other components (see, e.g., [87, 88]).

4. Estimation of Earth's magnetic field model

A necessary basis for any EMF model is the expansion coefficients in formulas (3) and (11)–(22), depending on the component under consideration. Building a model sometimes amounts to selecting a set of such coefficients. The main problem is therefore to select the coefficients such that the resulting potential describes the observed data as accurately as possible. The relation between the experimental results and the model parameters can be described as

$$\mathbf{d} = H(\mathbf{m}) + \mathbf{e}, \tag{23}$$

where $\mathbf{d}$ is the vector composed of field values experimentally determined in different regions of space, $\mathbf{m}$ is the vector of model parameters, $\mathbf{e}$ is the vector of measurement errors, and H is the operator that transforms the vector of model coefficients $\mathbf{m}$ into the vector of field values $\mathbf{d}-\mathbf{e}$. For example, in the problem of finding the potential of the main field, the vector of parameters involves the coefficients g_n^m and h_n^m, and the operator H is the transformation performed on the right-hand side of (3), whereas, for other field components, these are the corresponding expressions given by formulas (11)–(22). To obtain the vector $\mathbf{d}$, the entire available measurement area is divided into cells of preferably equal area, and the measured field values are then averaged. The spread of values is characterized by the covariance matrix C_m, and the spread of errors in $\mathbf{e}$, by the covariance matrix C_e.

Mathematically, finding the vector $\mathbf{m}$ of model parameters given the vector of initial data $\mathbf{d}$ is a typical ill-

posed inverse problem. To solve this problem in geomagnetism, the regularization (in most cases) and Bayesian (less often) approaches are traditionally used. Both include an iterative procedure for selecting model parameters **m** that satisfy Eqn (23), which is continued until a variable called the loss function either reaches some minimum value specified by the authors of the models or stops changing significantly.

4.1 Regularization approach

In the regularization approach, regularization terms are introduced that reflect some constraints imposed on the shape of the resultant potential. Such a term is included both in the loss function (see Eqn (25) below) and in the expression for the next-iteration vector of the model parameters (see Eqn (28) below).

The loss function can be written in the regularization approach as

$$\Phi(\mathbf{m}) = \big(\mathbf{d}-H(\mathbf{m})\big)^T C_e^{-1}\big(\mathbf{d}-H(\mathbf{m})\big) + \sum_{i=1}^{k} \lambda_i \mathbf{m}^T \Lambda_i \mathbf{m}\,, \quad (24)$$

where the first term characterizes the difference between model predictions and experimental data, taking their errors into account, and the second describes how well the parameter vector **m** satisfies the conditions specified by the ith regularization term, which represents additional constraints imposed on the parameter vector **m**. Here, λ_i is a regularization parameter that specifies the weight of the ith constraint relative to others and Λ_i is a regularization matrix describing the ith constraint. It is common practice to disregard cross-correlations of model parameters. In that case, the matrix C_e becomes diagonal, which significantly simplifies the calculations.

4.1.1 Regularization terms. Typically, the regularization term describes the smoothness requirements for the resultant potential in space and time at the boundaries of the domain of definition. For example, when considering the main field, smoothness is required for the distribution of the magnitude of the radial component of the field vector at the core–mantle boundary and over the entire time interval of the model. This requirement is expressed by the formula

$$\mathbf{m}^T \Lambda \mathbf{m} = \langle \ddot{B}^2 \rangle = \frac{1}{\Delta t}\int_{t_1}^{t_2}\int_{\Omega} \left|\frac{\partial^2 B_r}{\partial t^2}\right|^2 \mathrm{d}\Omega\,\mathrm{d}t\,, \quad (25)$$

where t_1 and t_2 define the boundaries of the time interval covered by the model, Δt is the duration of this time interval, and Ω is the interface between the core and the liquid mantle. For additional smoothing, a similar expression is used for the third derivative; however, the use of such a constraint on all of the time interval can distort information about short-period changes in the field, and it is therefore typically used only at the ends of the time interval of the model.

When considering the vector field **u** of flows at the core–mantle boundary (see Section 2.1.4.), in addition to similar spatial and temporal smoothness constraints on their distribution, restrictions on the nature of the dynamics of these flows are also used. The flows can be reduced to toroidal, geostrophic (i.e., dependent on the balance of the Coriolis force and the pressure gradient in the liquid core), and quasigeostrophic. For example, in the C^{3}FM model (see Table) for the geostrophic flows, the regularization term has the form [33]

$$\mathbf{u}^T \Lambda \mathbf{u} = \int_{\Omega} \big(\nabla_h(\mathbf{u}\cos\theta)\big)^2\,\mathrm{d}\Omega\,, \quad (26)$$

where θ is the colatitude.

Regularization terms for other field components include constraints on the smoothness of the lithospheric field on Earth's surface, minimization of the ionospheric field values on the night side, restrictions on the current density of the equatorial electrojet, and others. A description of similar regularization terms for the CM model can be found in [89]. There are also other variants of constraints: for example, in the gUFM model (see Table) the so-called Ohmic heating of the field is minimized (however, this parameter is now considered inaccurate and not working well).

4.1.2 Iteration procedure. To start the iteration procedure, an initial assumption about the values of the model parameters $\mathbf{m}_0$ is to be made; this is so-called a priori information. It can be chosen, for example, as a vector of parameters with arbitrary uniformly specified parameter values, or a third-party model. Often used in practice are either the IGRF model or a previous version of the relevant model itself (as, for example, in CHAOS models). In addition to the parameter values, a priori information includes the covariance matrix C_d and other statistical characteristics of the experimental data. Regularization terms are also often classified as a priori information.

A quite large class of models, including CM, CHAOS, BGS, Mag.num, and POMME, in their latest versions, implement the following standard scheme for solving the inverse problem. A priori values of the parameters are set equal to zero, and the covariance matrix is calculated from a comparison of the experimental data with the readings of the previous/test version of that model or of some other model. An iterative procedure is then launched, which can be implemented according to different schemes. Such schemes differ mainly in how the next-iteration vector of model parameters is calculated. As an example, we consider the Gaussian scheme

$$\mathbf{m}_{k+1} = \mathbf{m}_k + \big[J_k\big(H(\mathbf{m}_k)\big)^T C_e^{-1} J_k\big(H(\mathbf{m}_k)\big)\big]^{-1} \times \left[J_k\big(H(\mathbf{m}_k)\big)^T C_e^{-1}\big(\mathbf{d}-H(\mathbf{m}_k)\big) + \sum_{i=1}^{N}\lambda_i \Lambda_i \mathbf{m}_k\right], \quad (27)$$

where J_k is the Jacobian of the operator H for the kth vector of parameters.

Other schemes may include the method of least squares and renewing the weights of the data vector elements at each iteration step, depending on the magnitude of their deviations from the model and the distribution of errors.

The procedure stops, as already mentioned, when the loss function reaches minimum values. The choice of the minimality criterion, however, is a separate problem, which the authors of papers usually do not discuss.

4.2 Bayesian approach

In the Bayesian approach, instead of imposing constraints and requirements on the final form of the potential and the field for calculating the Gauss coefficients, they are assigned statistical characteristics, mainly covariance. The loss function and the expression for the parameter vector of the next iteration step

take the respective forms [90]

$$\Phi(\mathbf{m}) = \big(\mathbf{d} - H(\mathbf{m})\big)^T C_e^{-1}\big(\mathbf{d} - H(\mathbf{m})\big) + [\mathbf{m} - \mathbf{m}^b]^T C_m^{-1}[\mathbf{m} - \mathbf{m}^b], \quad (28)$$

and

$$\mathbf{m}_{k+1} = \mathbf{m}_k + \left[\nabla H(\mathbf{m}_k)^T C_e^{-1} \nabla H(\mathbf{m}_k) + C_b^{-1}\right]^{-1} \times \left[\nabla H(\boldsymbol{m}_k)^T C_e^{-1}\big(\mathbf{d} - H(\mathbf{m}_k)\big) - C_b^{-1}(\mathbf{m}_k - \mathbf{m}^b)\right]. \quad (29)$$

In these expressions, $\mathbf{m}^b$ is an estimate of the a priori mean of the parameter vector $\mathbf{m}$, C_b is its covariance matrix, and C_e is the a priori covariance matrix for the error vector $\mathbf{e}$. The second term in (28) characterizes the difference between the current vector of parameters and the a priori mean vector.

To calculate such a priori statistical characteristics of specific coefficients, a large number of them are played out based on the known characteristics of physical processes (see Section 4.3.1). The main advantage of the Bayesian approach is to be seen in the presence of statistical characteristics of the parameters of the resultant model, from which its error can be calculated. For example, the COV-OBS model (see Table), along with the Gauss coefficients, also gives their posterior covariance matrix.

4.3 Temporal dynamics and forecasts of EMF

Speaking of the temporal dynamics of the EMF components, we must distinguish between two types: periodic cyclic changes and stochastic changes. The accuracy and depth of their prediction depend on the specific type.

The first type of dynamics is represented, first and foremost, by the ionospheric, external, and tidal fields, whose very nature implies their cyclic changes. For such sources, the temporal dynamics are 'built into' the expression for the potential or into the definition of the expansion coefficients (see Eqns (15), (17), (18), and (22)).

Different approaches are used to describe the dynamics of field components that change stochastically (secular variation of the main field and dynamics of the external field associated with magnetospheric activity). The simplest approach is to use so-called snapshot models, where the decomposition parameters are estimated at individual points in time and the result is given by such a set of 'snapshots.' The model (collection of coefficients) obtained at that moment is used to reconstruct the field coefficients for the entire period until the next 'snapshot.' An example of such a model is provided by gUFM (see Table). This principle is also used in the CM model when describing the external field potential.

The second simple option is the interpolation between model parameters (i.e., collections of coefficients) obtained over adjacent time intervals. Such is the IGRF model, whose Gauss coefficients are calculated every five years and interpolated linearly between these points.

A more complex approach is to estimate the time series composed of model parameters using spline functions. In modern models, B-splines of different orders, usually the sixth, are used. Such a function can be written as

$$g_n^m(t) = \sum_{j=0}^{N} (g_n^m)_j \psi_j^l(t), \quad (30)$$

where N is the number of splines in the time interval, ψ_j^l is a function describing the jth spline, and l is the order of the spline. This method is currently the most common in describing the secular variation in the main field and is used in the CHAOS, CM, Mag.num, BGS, COV-OBS, GRIMM, and other models. Less commonly, it is used in describing the potential of other field components (for example, in the Mag.num (see Table), the coefficient g_1^0 of the induced field is parameterized in this way).

In the most sophisticated approaches, the statistical properties of time series composed of model parameters are analyzed. These methods include the ensemble method (see Section 4.3.1) used in the COV-OBS model (see Table), multivariate singular spectrum analysis (MSSA) used in the C^{3}FM model (see Table), and the Kalman filter.

4.3.1 Ensemble method. The ensemble method consists in statistical modeling over time of an arbitrary random process ϕ with specified characteristics. In problems of geomagnetism, such a random mathematical process must satisfy the statistical characteristics of real physical processes responsible for the secular variation in the main field (see Section 2.1). A characteristic manifestation of these processes is given by time series of Gauss coefficients and their time derivatives, as well as by the directly measured magnetic field vectors at different points on Earth. Random processes are usually represented in the form of an autoregressive model characterized by the correlation function $\rho(\tau)$, correlation time τ_c, variance σ^2, and expectation $E = \sigma^2\rho$. While different options are possible, we consider the example of an autoregressive model of the second kind (AR-2) used in the COV-OBS model (the choice of this model, together with other possible options, is justified in detail in [90]). The stochastic differential equation for this model is

$$\frac{\mathrm{d}^2\phi}{\mathrm{d}t^2} - \frac{3}{\tau_c^2}\phi = \epsilon(t), \quad (31)$$

where $\epsilon(t)$ denotes a random process realizing Gaussian white noise. The correlation function ρ and the expectation E are given by

$$\rho(\tau) = \left[1 + \sqrt{3}\,\frac{|\tau|}{\tau_c}\right]\exp\left(-\sqrt{3}\,\frac{|\tau|}{\tau_c}\right) \quad (32)$$

and

$$E(\tau) = E(0)\rho(\tau), \quad (33)$$

where $E(0)$ is expectation at the initial moment of time.

A priori values of $E(0)$ and τ_n are calculated from the values of the Gauss coefficients using the formulas

$$E_n(0) = \sigma_g^2(n) = \frac{1}{2n+1}\sum_{m=0}^{n}\left[g_n^m(t)^2 + h_n^m(t)^2\right] \quad (34)$$

and

$$\tau_n = \sqrt{\frac{\sigma_g^2(n)}{\sigma_{\dot{g}}^2(n)}}, \quad (35)$$

where $\sigma_g^2(n)$ is expectation of the nth-degree Gauss coefficients and $\sigma_{\dot{g}}^2(n)$ is the expectation of their time derivatives, defined similarly to (34). In the case of a large number of

coefficients, instead of the expectation E, the covariance matrix C is introduced. The correlation time characterizes the time period between the time series elements such that the correlation between them is half the one of the zeroth interval. It is therefore a characteristic of how far into the future a stochastic process can be predicted. For Gauss coefficients of the main field, τ_c ranges from a thousand years for second-degree harmonics to the order of several years for the 30th to 40th degrees. However, signals characterized by $\tau_c < 1$ year are filtered out when passing through the lithosphere and have zero autocorrelation on Earth's surface. The characteristic correlation time for $n = 13$, i.e., the approximate boundary for the detection of the main field, is 20 years, and characteristic times are 200 to 300 years.

The result of applying the method is an ensemble of models, which is a set of time series for each of the coefficients, played out randomly but satisfying the statistical characteristics of the process that controls them. Averaging the played out values of each of the coefficients at certain points in time allows obtaining the most suitable model at the corresponding moment and, importantly, reliable covariances of the model, i.e., information about statistical errors. Such information is unique to this method, because this information is lost in the classical approach associated with the use of regularization constraints imposed on the smoothness of the field in time. The ensemble method is used in cases where the magnitude and other statistical characteristics of the errors of the Gauss coefficients are important: for example, when studying the characteristics of flows in the liquid core [35] or in predicting the configuration of the main field in the future.

Forecasts based on the ensemble method rely on the statistical properties of the selected type of random process, the main one being the correlation time. Because it depends on the degree of the decomposition coefficient, the prediction limit is different for each coefficient and can range from several thousand years to one year.

The MSSA is based on identifying signals of different frequencies, large-scale trends, and noise in time data. The time series of model parameters are used to construct a matrix C whose elements are given by the covariance among model parameter values separated by different time periods,

$$c_{ij} = \frac{1}{N-\Delta}\sum_{t=1}^{N-\Delta} g_t\, g_{t+\Delta}\,, \tag{36}$$

where $\Delta = i - j$, g is now a time series of model parameters, and N is the number of values in the series.

In the case of a single-parameter analysis, the matrix C is analyzed further. In the multiparameter case, such matrices are compiled for each channel (i.e., time series of individual coefficients), combining into a large block matrix X,

$$X = \begin{pmatrix} C_{11} & C_{12} & \dots & C_{1L} \\ & C_{22} & \dots & C_{2L} \\ & & \ddots & \vdots \\ & & & C_{LL} \end{pmatrix}, \tag{37}$$

where L is the number of channels.

The set of eigenvectors $E^{k,l} : M_L$ reflects the directions in the multidimensional space along which the greatest variations are observed. By projecting the values of the time series onto the eigenvectors, the principal components A_t^k and the signal reconstruction $R_t^{l,k}$ are calculated as

$$A_t^k = \sum_{j=1}^{M}\sum_{l=1}^{L} Y_{t+j-1}^{l} E^{k,l}(j) \tag{38}$$

and

$$R_t^{l,k} = \frac{1}{M_t}\sum_{j=L_t}^{U_t} A^k(t-j+1)E^{l,k}(j)\,. \tag{39}$$

The behavior of eigenvectors over time is characterized by different periodicities and reflects the dynamics of the magnetic field, and the values of neighboring eigenvectors allow determining noise and trends. Knowledge of these characteristics also allows predicting the magnetic field configuration. This analysis is also used in predicting the magnetized fluid flows at the core–mantle boundary, for example, in the C^{3}FM model (see Table).

4.3.2 Kalman filter. This technique, used to correct and refine time series of the Gauss coefficients in geomagnetism, is an alternative to the use of splines when describing the dependence of the coefficients on time. In applying the Kalman filter, the problem of finding model parameters for a number of successive time intervals is divided into three stages: analysis, forecast, and smoothing, which are repeated for each time interval. At the analysis stage, the standard inverse problem is solved for the current time interval. At the forecast stage, a model forecast is made for the next time period based on the current one. This forecast is typically based on a random process simulation (see Section 4.3.1). The posterior (i.e., predicted) values of the model parameters and their covariances become a priori information for the first step of the second time period. At the smoothing stage, the model parameters for the preceding time period are adjusted based on the values of the current model. A good example of the use of the Kalman filter is the model described in [91].

5. Models of Earth's magnetic field

As already noted, the currently accepted form of modeling EMF in Earth's inner magnetosphere originates from Gauss's model. By that time, other models had existed, for example, those assuming the presence of more than two poles, but Gauss's model proved to be the most successful and quickly gained recognition. In this model, the potential of the entire observed field was decomposed into harmonics up to only the fourth degree. But with the increase in the number of observations, geomagnetic stations, and magnetic surveys, the accuracy of observations also increased, and different models began appearing, initially based on maps of magnetic declinations, inclinations, and magnetic field strength. By the mid-1960s, due to the abundance of experimental data, a number of EMF models already existed, based on data of a very diverse nature [92]. In addition to geomagnetic observatories and repeat stations, they relied heavily on global marine magnetic surveys, as well as on continental aerial surveys conducted by the USSR, the USA, Japan, and other countries. Tables 7 and 8 in [93] can give an idea of the development and number of models existing at that time.

Most of the models, however, implemented the same idea of representing the field as a decomposition into spherical harmonics, which motivated the task to unify and standardize them. In 1968, under the auspices of the International

Association of Geodesy and Aeronomy, the first version of the IGRF (International Geomagnetic Reference Field) model was presented, based on 'averaging' over four candidate models [94] and describing the field for the epoch of 1965. The first version included models prepared by the Goddard Space Flight Center and the Massachusetts Air Force Research Laboratory (USA), based on data from American magnetic surveys and from the OGO-2 spacecraft; the Institute of Geological Sciences of the Royal Greenwich Observatory in London based on data from British magnetic surveys; and the Institute of Terrestrial Magnetism, the Ionosphere, and Radio Wave Propagation (IZMIRAN) in Troitsk based on data from Kosmos-49 and magnetic surveys conducted in the Soviet Union. A new version of the model, i.e., a new set of coefficients, appeared 7 years later, and it corresponded to a time period separated by 10 years from that of the first coefficients. At that time, it became clear that this was too long an interval for interpolation, and it was subsequently decided to update the model at a frequency of five years. The early history of the development of the IGRF model is described in review [95].

This basic approach is preserved to this day, although the model 'averaging' algorithm is being improved all the time (its existing version is described in [96, 97]). At the same time, the number of scientific teams submitting their models as candidates has grown to 15. In what follows, we describe the main models that exist today.

5.1 Models of EMF in the near magnetosphere

The *IGRF* (*International Geomagnetic Reference Field*) model contains three types of coefficients: IGRF, DGRF (definitive geomagnetic reference field), and SV (secular variation). IGRF is the set of coefficients at the time a model is formulated; for example, the modern version is IGRF2020, which will later be adjusted as new data is accumulated and converted into DGRF2020. DGRF is a set of adjusted coefficients that appears in the next version of the model relative to the preceding one; for example, in the current version, the DGRF coefficients are available for the period from 1900 to 2015 with a five-year increment. SV is a set of secular variation coefficients in the form of time derivatives of the Gauss coefficients; they are used to forecast the field five years ahead until the next version is prepared. The IGRF model fundamentally describes only the main field and its secular variation, and therefore, to eliminate the addition of a lithospheric signal as much as possible, the degree of decomposition is limited to 13 for the modern era and 8 to 10 for periods prior to 2000.

WMM (*World Magnetic Model*) is another model of Earth's main field and its secular variation. It is created and maintained jointly by the National Center for Environmental Information (NCEI), National Oceanic and Atmospheric Administration (NOAA), USA, and the British Geological Survey (BGS). The model primarily aims at commercial use in navigation, and, hence, in addition to the standard output of field components, it also provides some technical parameters that are nonstandard for other models, such as notes on the blackout zone in the polar region where magnetic declination measurements become unreliable. The commercial orientation of the model also determines its 'prospectfulness' (in contrast to retrospective models): it describes only the configuration of the field at the current moment and the forecast of its secular variation for five years ahead. In addition, corrections to the original coefficients are released each year within these five subsequent years. From the standpoint of model construction, like the IGRF, it is made of candidate models, but in this case there are two candidate models, represented by NCEI and BGS.

CHAOS (*CHAMP, Ørsted, and SAC-C*) began to be developed in 2006 by the Technical University of Denmark based on data from the magnetometers whose names form the name of the model [98] and is currently available in its seventh version. In recent years, the model has been one of the main ones, regularly submitting its child models to IGRF candidates. In previous versions, the model existed in two versions (for example, this applies to CHAOS versions 4 [84] through 6 [99]), with the prefix l or h. The l-version of the model (low) described the harmonic coefficients of lower degrees (they included the main field and the large-scale component of the lithospheric field), and the h-one (high), the higher degrees (the small-scale component of the lithospheric field). In the most recent version, the coefficients of higher degrees (up to 185) are placed in a separate model of the lithospheric field LCS-1 [88], while, in the main model, the lithospheric field is represented only up to the 50th order, as shown in the table.

CM (*Comprehensive Model*), developed by the Geodesy and Geophysics Laboratory, Goddard Space Flight Center (NASA, USA), is the main model that implements the comprehensive approach. Unlike most of the models on this list, the CM began to be developed before the era of massive high-precision satellite measurements of the field: the first GSFC version (12/93) was released in 1993. The first versions were based on MagSat and POGO data, but the latest versions of the model cover the time interval from 1999 to the present and are based on data from the CHAMP and Swarm devices. There is also a version of the model based solely on the Swarm CIY4 data [89]. As regards its special features, it is worth noting that this model is currently the only one that describes the tidal components of the field.

GFZ models are a series of models of the Helmholtz Centre Potsdam, German Research Centre for Geosciences (GFZ), and include the Mag.num and GRIMM models, and also the first versions of the POMME model. All models are typical representatives of the sequential approach. It is worth noting, however, that the first versions of the GRIMM model were based on the comprehensive approach and included a description of the ionospheric fields of the E- and F-regions.

BGS (*British Geological Survey*) models place the main emphasis on the most accurate description of the lithospheric field, because their main application is practical: mine drilling and geological exploration. In describing the main field, standard approaches to parameterization, selection, and data approximation are used.

COV-OBS. In this model, being developed at the University of Grenoble since 2013 [90], the ensemble method and the Bayesian approach are implemented to solve the inverse problem in the model approximation. The main distinctive feature of the model is that its result, in addition to the main field expansion coefficients themselves, also includes their a posteriori covariance matrix, which characterizes the model error. In addition, because the authors of the model attempt to statistically describe the random processes characterizing the secular variation in the field, they use the maximum available interval of accurate data. Thus, the model covers one of the longest time intervals, from 1840 to 2020, and also naturally includes a field forecast whose range depends on the degree of decomposition.

gUFM. The model was developed at the University of Leeds, UK. It is a historical snapshot model of the magnetic field at the core–mantle boundary, covering the period from 1600 to 2000. Although models for that historical period were being developed earlier [100], today it is unique in terms of this parameter. However, the model returns not a set of Gauss coefficients but the components of the magnetic field vector on the surface of the core, which limits its use. The most notable feature of the model, of course, is the historical data used. Undoubtedly, much work has been done to collect and digitize historical magnetic declination measurements from data of ship logs [56]. Also, to use this data, the authors of the model needed to take into account specific errors associated, for example, with the procedure for dead reckoning when planning a route by sailors. In addition, because before the beginning of the 19th century scientists were able to measure the direction of the field but not its strength, the early data do not allow establishing the absolute values of the field but only its geometric configuration. To solve this problem, the authors of the model extrapolate the value of Earth's magnetic dipole measured since the 1840s into the past and use it as a scale factor. In addition to the gUFM model itself, there is also the gUFM-SAT model [101] based on data from the CHAMP and Ørsted magnetometers and covering the period 2000–2010. However, it is connected with the gUFM model only by the use of ohmic heating at the core–mantle boundary as a regularization term.

C^3FM is a model of the University of Strasbourg. Its main feature is that, in solving the inverse problem, the parameters of the decomposition of the main field (classical approach) and the vector field of flows in the liquid core (kinematical approach) are co-estimated. As the experimental data, the authors of the model fundamentally use only secular variations in the magnetic field vector measured at different points, and the satellite data for synchronization are presented in the form of virtual observatories evenly distributed over the surface of the globe. The field forecast in the model is MSSA-based, and is also presented in two versions: as series of values of the magnetic field vector at different points and as series of values of flows in the core calculated from values of the secular variation.

Kalmag is a new model of the University of Potsdam where the comprehensive approach is implemented. This model is the second modern one, after the CM, in which the ionospheric field and its induced component are parameterized and co-estimated. Other features include a very detailed decomposition of the external field potential (up to the 15th degree), and the most detailed description of the lithospheric component for a model not aimed at exclusively describing the lithospheric field.

In the table, we present the basic characteristics of the main currently existing magnetic field models.

Other models. In addition to those described above, it is also worth mentioning models that are left outside the scope of this description. First of all, it is worth noting the EMM [102] and HDGM [103] models, which, although primarily aimed at a detailed description of the lithospheric field up to harmonics of the highest degrees (790), nevertheless describe both the main field and its secular variation. Also worth noting is Stefan Maus's POMME model [104], the recently released model of the NCEI BOUME research wing [105], the IGRF+ model extended back to 1600 with the addition of the gUFM model [106], and the original EMF model built on the Swarm data [107]. In addition, a number of teams calculate their main field decomposition parameters without formalizing this into a separate model, but proposing them as candidate models for the IGRF (see, e.g., [108]). Magnetohydrodynamical core models not discussed here (see, e.g., [109]) also present their candidate SV models within the IGRF framework.

5.2 Assessing model accuracy

Although comparisons of models and their evaluation are beyond the scope of this review, it is nevertheless worth giving an idea of what the creators base the models themselves on when speaking about the correctness in describing the field. This is first of all the distribution of the difference between the model prediction and directly measured values (that have undergone appropriate selection): its mean deviation (which characterizes the systematic error) and the standard RMS deviation, which characterizes the spread of values. These values typically depend on the geographic area, the source of the experimental data, and other parameters. For example, both RMS and mean deviation are on average larger for polar areas than for equatorial and temperate regions. This is due to the complexity of data selection in this area and, accordingly, greater contamination by signals from ionospheric and external currents. Also, the error in comparing with Swarm data is usually less than with older CHAMP, Ørsted, or SAC-C data. For the CM model, the error data are also divided into day and night sides: there are higher errors in the former. The characteristic value of the average deviation in almost all modern models ranges from ~ 0.01 nT in the equatorial region to $\sim$ 1–2 nT in the polar region. The RMS can vary: for example, for the CHAOS model, it ranges from 1.5–2 nT in nonpolar regions (depending on the instrument whose measurements were used) to 3 nT in polar regions. For the Mag.num model, the RMS already reaches $\sim$ 30–40 nT for polar regions. In the CM model, the highest value is observed on the illuminated side. A very detailed study of errors in their main field model was carried out by the authors of WMM [110], where errors associated with the influence of the lithospheric field, external field disturbances, etc. were examined in detail; the total error was 129 nT for the total field strength and from 86 to 146 nT for the components. An error larger than in other models apparently occurs because, unlike in those models, only the main field is considered here, and all other sources are regarded as sources of error.

Another typical test is to compare measurements at specific geomagnetic observatories with time series compiled from model readings for a corresponding point in space during the time studied (see Fig. 7 in [27]), or to compare the time series compiled from the Gauss coefficients of the model and their derivatives (see Figs 3 and 4 in [111]).

6. Conclusions

We have discussed the scientific and applied aspects of EMF modeling in the near magnetosphere, which are useful primarily for those who apply such models in practice to achieve scientific results in their fields, primarily in the field of cosmic rays. The principles of model building, mathematical tools, experimental measurements underlying the models, and various field sources are analyzed in detail. Such data helps us to understand the range of applicability of models, their limitations, and uncertainties in their results, which are usually not stated manifestly, not least because of the complexity of their nature. Moreover, for different physical

problems, uncertainties of different natures may be important, associated with the presence of field sources not described by the model, its mathematical tools, or other aspects. Having described all important components of the models (field sources, experimental data, and mathematical tools), we discussed the main characteristics of most modern models of the magnetic field in Earth's inner magnetosphere in detail and collected them in a table.

7. Data sources

All versions of the CHAOS and COV-OBS model, the latest versions of the CM, and the original Swarm, CHARM, and Ørsted models can be downloaded from the website of the Technical University of Denmark at https://www.space.dtu.dk/english/research/scientific_data_and_models/magnetic_field_models. The latest versions of the WMM, IGRF, BOUME, and POMME-10 models and a number of lithospheric and ionospheric field models are posted on the website of the CIROS/NCEI geomagnetism group at https://geomag.colorado.edu/geomagnetic-and-electric-field-models.html. Source codes for all versions of the GRIMM models, Gauss coefficients for the Mag.num and C^3FM models, as well as a series of paleomagnetic models are available on the website of the Potsdam Research Center at https://www.gfz-potsdam.de/en/section/geomagnetism/data-products-services/geomagnetic-field-models/. The BGS model (and the latest versions of WMM and IGRF) is available on the British Geological Survey page at https://geomag.bgs.ac.uk/research/modelling/modelling.html. The Kalmag model in the form of Gauss coefficients of the main and lithospheric fields, as well as secular variations, is available at https://ionocovar.agnld.uni-potsdam.de/Kalmag/. All versions of the POMME model are posted on Stefan Maus's page at https://geomag.us/models/index.html. The source code for gUFM is available on the GitHub platform at https://github.com/martinrehfeld/gufm1-webservice. The IGRF model in various forms, including older versions, is also available on its Internet page at https://www.ngdc.noaa.gov/IAGA/vmod/igrf.html.

Acknowledgments. The research was supported by the Russian Science Foundation, grant no. 19-72-10161, https://rscf.ru /project/19-72-10161/.

References

1. Adriani O et al. *Astrophys. J. Lett.* **799** L4 (2015)
2. Fiandrini E *J. Geophys. Res.* **109** A10214 (2004)
3. Karelin A V et al. *J. Exp. Theor. Phys.* **117** 62 (2013); *Zh. Eksp. Teor. Fiz.* **144** 75 (2013)
4. Smart D F, Shea M A *Adv. Space Res.* **36** 2012 (2005)
5. Leske R A et al. *J. Geophys. Res.* **106** 30011 (2001)
6. Bruno A et al. *Adv. Space Res.* **60** 788 (2017)
7. Adriani O et al. *Astrophys. J. Lett.* **801** L3 (2015)
8. Ginet G P et al. *Space Sci. Rev.* **179** 579 (2013)
9. Selesnick R S, Looper M D, Mewaldt R A *Space Weather* **5** S04003 (2007) https://doi.org/10.1029/2006SW000275
10. Bakaldin A V, Voronov S A *Instrum. Exp. Tech.* **61** 725 (2018); *Prib. Tekh. Eksp.* (5) 102 (2018)
11. Gvishiani A D, Luk'yanov R Yu, Solov'ev A A *Geomagnetism: ot Yadra Zemli do Solntsa* (Geomagnetism: from the Earth's Core to the Sun) (Moscow: RAN, 2019)
12. Korte M, Mandea M *Geochem. Geophys. Geosyst.* **20** 3801 (2019)
13. Sokoloff D D, Stepanov R A, Frick P G *Phys. Usp.* **57** 292 (2014); *Usp. Fiz. Nauk* **184** 313 (2014)
14. Sokoloff D D *Phys. Usp.* **58** 601 (2015); *Usp. Fiz. Nauk* **185** 643 (2015)
15. Mitchell A C *Terr. Magn. Atmos. Electr.* **37** (2) 105 (1932)
16. Stern D P *Rev. Geophys.* **27** (1) 103 (1989)
17. Cawood J *ISIS* **70** (4) 493 (1979)
18. Elsasser W M *Phys. Rev.* **55** 489 (1939)
19. Gordin V M *Ocherki po Istorii Geomagnitnykh Izmerenii* (Essays on the History of Geomagnetic Measurements) (Moscow: IFZ RAN, 2004)
20. Tsyganenko N A *Ann. Geophys.* **31** 1745 (2013)
21. Wicht J, Sanchez S *Geophys. Astrophys. Fluid Dyn.* **113** (1–2) 2 (2019)
22. Kuslits L et al. *Acta Geod. Geophys.* **55** 347 (2020)
23. Finlay C C et al. *Space Sci. Rev.* **155** 177 (2010)
24. Finlay C C, Aubert J, Gillet N *Nat. Commun.* **7** 10422 (2016)
25. Valet J-P, Fournier A *Rev. Geophys.* **54** 410 (2016)
26. Aleksandrin S Yu et al., in *Proc. of the 34th Intern. Cosmic Ray Conf., ICRC2015, 30 July–6 August, 2015, The Hague, The Netherlands*; *PoS* **236** 89 (2016)
27. Finlay C C et al. *Earth Planets Space* **72** 156 (2020)
28. Kakad A, Kakad B *Adv. Space Res.* **69** 2142 (2022)
29. Aubert J, Finlay C C *Nat. Geosci.* **12** 393 (2019)
30. Holme R, in *Treatise in Geophysics* Vol. 8 *Core Dynamics* (Ed.-in-Chief G Schubert) (Amsterdam: Elsevier, 2007) p. 107
31. Roberts P H, Scott S *J. Geomagn. Geoelectr.* **17** (2) 137 (1965)
32. Lesur V et al. *Earth Planets Space* **62** 503 (2010)
33. Wardinski I et al. *Earth Planets Space* **72** 155 (2020)
34. Hulot G, Mouël J L Le, Wahr J *Geophys. J. Int.* **108** 224 (1992)
35. Gillet N, Pais M A, Jault D *Geochem., Geophys. Geosyst.* **10** (6) (2009)
36. Dunlop D J, Özdemir Ö, in *Treatise in Geophysics* Vol. 5 *Geomagnetism* (Ed. G Schubert) (Amsterdam: Elsevier, 2007) p. 277
37. Lowes F J *Geophys. J. Int.* **36** 717 (1974)
38. Ganushkina N Yu, Liemohn M W, Dubyagin S *Rev. Geophys.* **56** 309 (2018)
39. Samsonov A A et al. *J. Geophys. Res. Space Phys.* **124** 4049 (2019)
40. Coxon J C et al. *J. Geophys. Res. Space Phys.* **121** 4027 (2016)
41. Hamilton B et al. *Earth Planets Space* **67** 69 (2015)
42. Sabaka T J, Olsen N, Purucker M E *Geophys. J. Int.* **159** 521 (2004)
43. Lesur V et al. *Geophys. J. Int.* **173** 382 (2008)
44. Yamazaki Y, Maute A *Space Sci. Rev.* **206** 299 (2017)
45. Sabaka T J, Olsen N, Langel R A *Geophys. J. Int.* **151** (1) 32 (2002)
46. Tyler R H et al. *Earth Planets Space* **69** 156 (2017)
47. Kuvshinov A V *Surv. Geophys.* **29** 139 (2008)
48. Kuvshinov A et al. *Earth Planets Space* **73** 67 (2021)
49. Alekseev D, Kuvshinov A, Palshin N *Earth Planets Space* **67** (1) 108 (2015)
50. Grayver A V, Olsen N *Geophys. Res. Lett.* **46** 4230 (2019)
51. Velímský J, Šachl L, Martinec Z *Earth Planet. Sci. Lett.* **509** 47 (2019)
52. Torres C E, Calisto I, Figueroa D *Pure Appl. Geophys.* **176** 3167 (2019)
53. Minami T *Surv. Geophys.* **38** 1097 (2017)
54. Velímský J et al. *Ocean Sci.* **17** 383 (2021)
55. Jonkers A R T, in *Encyclopedia of Geomagnetism and Paleomagnetism* (Eds D Gubbins, E Herrero-Bervera) (Dordrecht: Springer, 2007) p. 355
56. Jonkers A R T, Jackson A, Murray A *Rev. Geophys.* **41** 1006 (2003)
57. Jackson A, Jonkers A R T, Walker M R *Philos. Trans. R. Soc. London A* **358** 957 (2000)
58. Malin S R C, Bullard E *Philos. Trans. R. Soc. London A* **299** 357 (1981)
59. Alexandrescu M, Courtillot V, Le Mouël J-L *Phys. Earth Planet. Int.* **98** 321 (1996)
60. Ptitsyna N G et al. *Geomagn. Aeron.* **53** 684 (2013)
61. Malin S R C, Barraclough D R *Q. J. R. Astron. Soc.* **32** 279 (1991)
62. O'Hara J G *Notes Rec. R. Soc. Lond.* **38** (1) 17 (1983)
63. Soloviev A, Lesur V, Kudin D *Earth Planets Space* **70** (1) 16 (2018)
64. Love J J, Chulliat A *Eos, Trans. Am. Geophys. Union* **94** (42) 373 (2013)
65. Macmillan S, Olsen N *Earth Planets Space* **65** (11) 1355 (2013)
66. Chulliat A, in *Geomagnetism, Aeronomy and Space Weather* (Eds M Mandea et al.) (Cambridge: Cambridge Univ. Press, 2019) p. 54

67. Kauristie K et al. *Space Sci. Rev*. **206** (1–4) 61 (2017)
68. Benkova N P, Dolginov S S *IAGA Bull*. **28** 75 (1971)
69. Dolgin Sh Sh et al. *Geomagn. Aeron*. **12** 1046 (1972)
70. Cain J C, Sweeney R, in *Fourth Intern. Symp. on Equatorial Aeronomy, 1972*
71. Mobley F et al. *IEEE Trans. Magn*. **16** 758 (1980)
72. Neubert T et al. *Eos Trans. AGU* **82** (7) 81 (2001)
73. Jørgensen P S, Merayo J M G, Risbo T *Sensors Actuators A* **95** (1) 1 (2001)
74. Friis-Christensen E, Lühr H, Hulot G *Earth Planets Space* **58** 351 (2006)
75. Olsen N et al. *Earth Planets Space* **72** (1) 48 (2020)
76. Langel R A et al. *J. Geomagn. Geoelectr*. **40** 1103 (1988)
77. Shen X et al. *Sci. China Technol. Sci*. **61** 634 (2018)
78. Jianing Z et al. *Front. Earth Sci*. **10** 866438 (2022)
79. Califf S et al. *Earth Planets Space* **74** (1) 37 (2022)
80. Blagau A et al. *Acta Astronaut*. **195** 456 (2022)
81. Swarm data, The European Space Agency, https://earth.esa.int/eogateway/missions/swarm/data
82. Magnetic satellites data, DTU space, https://www.space.dtu.dk/english/research/scientific_data_and_models/magnetic_satellites
83. CSES data, https://leos.ac.cn/#/home
84. Olsen N et al. *Geophys. J. Int*. **197** 815 (2014)
85. Thomson A W P, Lesur V *Geophys. J. Int*. **169** 951 (2007)
86. Finlay C C et al. *Space Sci. Rev*. **206** 157 (2017)
87. Thébault E et al. *Space Sci. Rev*. **155** 95 (2010)
88. Olsen N et al. *Geophys. J. Int*. **211** 1461 (2017)
89. Sabaka T J et al. *Earth Planets Space* **70** (1) 130 (2018)
90. Gillet N et al. *Geochem. Geophys. Geosyst*. **14** 766 (2013)
91. Ropp G et al. *Earth Planets Space* **72** (1) 153 (2020)
92. Cain J C *Radiation Trapped in the Earth's Magnetic Field* (Dordrecht: Springer, 1966)
93. Cain J C et al. *J. Geophys. Res*. **70** (15) 3647 (1965)
94. Zmuda A J *Eos Trans. AGU* **52** (2) 60 (1971)
95. Langel R A *J. Geomagn. Geoelectr*. **44** 679 (1992)
96. Alken P et al. *Earth Planets Space* **73** (1) 48 (2021)
97. Thébault E et al. *Earth Planets Space* **67** (1) 112 (2015)
98. Olsen N et al. *Geophys. J. Int*. **166** 67 (2006)
99. Finlay C C et al. *Earth Planets Space* **68** (1) (2016)
100. Yukitake T *J. Geomagn. Geoelectr*. **23** (1) 11 (1971)
101. Finlay C C et al. *Geophys. J. Int*. **189** (2) 761 (2012)
102. NCEI 2017, https://www.ncei.noaa.gov/products/enhanced-magnetic-model
103. Nair M et al., in *Offshore Technology Conf. Proc., Aug. 2021*
104. POMME-11, CIRES, https://geomag.us/models/pomme11.html
105. BOUME, CIRES, https://geomag.colorado.edu/geomagnetic-and-electric-field-models/2-uncategorised/128-boumme.html
106. CIRES, https://geomag.colorado.edu/online-calculators.html
107. Olsen N et al. *Geophys. Res. Lett*. **42** 1092 (2015)
108. Petrov V G, Bondar T N *Earth Planets Space* **73** (1) 46 (2021)
109. Minami T et al. *Earth Planets Space* **72** (1) 136 (2020)
110. Chulliat A et al. "The US/UK World Magnetic Model for 2020–2025", Technical Report (Boulder, CO: National Centers for Environmental Information, NOAA, 2020)
111. Sabaka T J et al. *Earth Planets Space* **72** 80 (2020)
112. Alken P et al. *Earth Planets Space* **73** 49 (2021)
113. Rother M et al. *Earth Planets Space* **73** 50 (2021)
114. Brown W J et al. *Earth Planets Space* **73** 42 (2021)
115. Huder L et al. *Earth Planets Space* **72** 160 (2020)
116. Baerenzung J et al. *Earth Planets Space* **72** 163 (2020)
117. Maus S et al. *Earth Planets Space* **62** 729 (2010)